

This discussion paper is/has been under review for the journal *Atmospheric Chemistry and Physics (ACP)*. Please refer to the corresponding final paper in *ACP* if available.

Meteoric ablation

T. Vondrak et al.

A chemical model of meteoric ablation

T. Vondrak¹, J. M. C. Plane¹, S. Broadley¹, and D. Janches²

¹School of Chemistry, University of Leeds, Leeds, UK

²NorthWest Research Associates, CoRA Division, Boulder, CO, USA

Received: 23 May 2008 – Accepted: 3 July 2008 – Published: 30 July 2008

Correspondence to: J. M. C. Plane (j.m.c.plane@leeds.ac.uk)

Published by Copernicus Publications on behalf of the European Geosciences Union.

Title Page

Abstract

Introduction

Conclusions

References

Tables

Figures

◀

▶

◀

▶

Back

Close

Full Screen / Esc

Printer-friendly Version

Interactive Discussion



Abstract

Most of the extraterrestrial dust entering the Earth's atmosphere ablates to produce metal vapours, which have significant effects on the aeronomy of the upper mesosphere and lower thermosphere. A new Chemical Ablation Model (CAMOD) is described which treats the physics and chemistry of ablation, by including the following processes: sputtering by inelastic collisions with air molecules before the meteoroid melts; evaporation of atoms and oxides from the molten particle; diffusion-controlled migration of the volatile constituents (Na and K) through the molten particle; and impact ionization of the ablated fragments by hyperthermal collisions with air molecules. Evaporation is based on thermodynamic equilibrium in the molten meteoroid (treated as a melt of metal oxides), and between the particle and surrounding vapour phase. The loss rate of each element is then determined assuming Langmuir evaporation. CAMOD successfully predicts the meteor head echo appearance heights, observed from incoherent scatter radars, over a wide range of meteoroid velocities. The model also confirms that differential ablation explains common-volume lidar observations of K, Ca and Ca^+ in fresh meteor trails. CAMOD is then used to calculate the injection rates into the atmosphere of a variety of elements as a function of altitude, integrated over the meteoroid mass and velocity distributions. The most abundant elements (Fe, Mg and Si) have peak injection rates around 85 km, with Na and K about 8 km higher. The more refractory element Ca ablates around 82 km with a Na:Ca ratio of 4:1, which does therefore not explain the depletion of atomic Ca to Na, by more than 2 orders of magnitude, in the upper mesosphere. Diffusion of the most volatile elements (Na and K) does not appear to be rate-limiting except in the fastest meteoroids. Non-thermal sputtering causes ~35% mass loss from the fastest (~60–70 km s⁻¹) and smallest (10^{-17} – 10^{-13} g) meteoroids, but makes a minor contribution to the overall ablation rate.

ACPD

8, 14557–14606, 2008

Meteoritic ablation

T. Vondrak et al.

Title Page

Abstract

Introduction

Conclusions

References

Tables

Figures

◀

▶

◀

▶

Back

Close

Full Screen / Esc

Printer-friendly Version

Interactive Discussion



1 Introduction

There are two principal sources of meteoroids in the Earth's atmosphere (Ceplecha et al., 1998; Williams, 2002). First are the dust trails produced by sublimating comets as they orbit the sun, which are the origin of meteor showers such as the Perseids and Leonids. Second are fragments from the asteroid belt beyond Mars, and dust particles from long-decayed cometary trails. These give rise to the continuous input of sporadic meteoroids which provides a much greater mass flux than the showers (Ceplecha et al., 1998; Williams, 2002). Because of their very high entry velocities, meteoroids undergo rapid frictional heating by collision with air molecules, and their constituent minerals subsequently vaporize. This provides the dominant source of various metals and silicon in the upper atmosphere, which are manifest as layers of neutral metal atoms (Na, Fe, Ca etc.) between about 80 and 105 km, and as sporadic *E* layers between 90 and 140 km (Plane, 2003). Below 85 km the metals form compounds such as oxides and carbonates which condense to form meteoric smoke particles (e.g. Hunten et al., 1980; Kalashnikova et al., 2000; Saunders and Plane, 2006). These nm-sized particles most probably provide ice nuclei for the formation of noctilucent clouds in the summer high latitude mesosphere (Megner et al., 2006), and polar stratospheric clouds in the wintertime polar stratosphere (Curtius et al., 2005).

The input flux of meteoroids into the atmosphere is rather uncertain, because no single technique can observe particles over the mass range from about 10^{-12} to 1 g, which make up the bulk of the incoming material (Ceplecha et al., 1998). In addition, meteoroids which originate within the solar system (the vast majority) have a large range of entry velocities, from 11.5 km s^{-1} for a particle in the same orbit as the Earth, to 72.5 km s^{-1} for a particle in a retrograde orbit (Baggaley, 2002). Until the 1990s, a commonly assumed figure for the daily mass input was 44 t d^{-1} , averaged over the entire Earth (Hughes, 1978). This estimate was made by extrapolating between visual meteors (mass $>10 \text{ mg}$) and satellite impact data (mass $<1 \mu\text{g}$), and ignoring indications of a somewhat lower flux from measurements made by conventional meteor

Meteoric ablation

T. Vondrak et al.

Title Page

Abstract

Introduction

Conclusions

References

Tables

Figures



Back

Close

Full Screen / Esc

Printer-friendly Version

Interactive Discussion



Meteoritic ablation

T. Vondrak et al.

[Title Page](#)[Abstract](#)[Introduction](#)[Conclusions](#)[References](#)[Tables](#)[Figures](#)[◀](#)[▶](#)[◀](#)[▶](#)[Back](#)[Close](#)[Full Screen / Esc](#)[Printer-friendly Version](#)[Interactive Discussion](#)

radars (these instruments measure specular reflections from the ion trail created in the atmosphere by the ablating meteoroid) (Hughes, 1997). More recently, the analysis of small particle impact craters on the Long Duration Exposure Facility (LDEF), an orbital impact detector placed on a spacecraft for several years, has yielded an estimate of $110 \pm 55 \text{ t d}^{-1}$ (Love and Brownlee, 1993; McBride et al., 1999). The median mass of the incoming dust particles was deduced to be $\sim 10 \mu\text{g}$ with a mean entry velocity of about 18 km s^{-1} . However, it is important to note that the LDEF experiment measured crater size, which was treated as a proxy for particle kinetic energy. Hence, the particle velocity distribution had to be assumed in order to produce the mass distribution.

In the last few years, high-powered large aperture (HPLA) radars have reported direct observations of the meteor head echo (i.e. the ball of plasma around the ablating particle as it descends through the atmosphere). This enables measurements of the direction of the line-of-sight velocity, deceleration and meteoroid mass to be made (e.g. Pellinen-Wannberg and Wannberg, 1994; Close et al., 2000; Janches et al., 2000). The observed mass distribution is shifted to smaller mass ranges (median mass $\approx 1 \mu\text{g}$) compared to the LDEF results, and the total incoming mass is about 1 order of magnitude lower than the LDEF estimate. The mean entry velocity also seems to be significantly higher, around $40\text{--}50 \text{ km s}^{-1}$ (Mathews et al., 2001). However, the magnitude of the head echo is highly dependent on the meteoroid mass and velocity, so that this technique is biased to faster particles (Dyrud et al., 2005). Each HPLA radar is also sensitive to a particular mass range (Janches et al., 2007).

The mass flux has also been estimated in other ways. Single-particle analyses of stratospheric aerosol have shown that half of the particles in the lower stratosphere contain 0.5 to 1.0 weight percent meteoric iron by mass, requiring a total extraterrestrial flux of between 20 and 100 t d^{-1} (Cziczo et al., 2001). Measurements of the accumulation of Ir and Pt in polar ice cores have been used to deduce a mass flux of $40 \pm 16 \text{ t d}^{-1}$ (Gabrielli et al., 2004); measurements of supermagnetism from cosmic Fe in ice cores indicate a flux of $35 \pm 10 \text{ t d}^{-1}$ (Lanci et al., 2007). Finally, a model of the mesospheric Na layer requires a flux of $10\text{--}30 \text{ t d}^{-1}$ to match lidar observations of the

Meteoritic ablation

T. Vondrak et al.

[Title Page](#)[Abstract](#)[Introduction](#)[Conclusions](#)[References](#)[Tables](#)[Figures](#)[◀](#)[▶](#)[◀](#)[▶](#)[Back](#)[Close](#)[Full Screen / Esc](#)[Printer-friendly Version](#)[Interactive Discussion](#)

layer (Plane, 2004). A consensus around $20\text{--}40\text{ t d}^{-1}$ has therefore emerged in the last 5 years, but this remains highly uncertain and is in any case a crude average that does not take account of seasonal and latitudinal variations (Janches et al., 2006; Fentzke and Janches, 2008).

Because of their very high entry velocities, meteoroids undergo rapid frictional heating by collision with air molecules, and their constituent minerals subsequently vaporize. The physics of this process has been treated in detail by several investigators. The frictional heating is balanced by radiative losses and by the absorption of heat energy through temperature increases, melting, phase transitions, and vaporization. In order to calculate these terms, parameters such as the meteoroid shape, density, and composition are needed. The question of composition has been discussed in detail recently (Rietmeijer, 2000, 2002). There is some uncertainty because of the great variability in composition of the different types of meteorites (Rietmeijer, 2000). Furthermore, it may be that the composition of the meteoroids that ablate in the upper atmosphere is different from that of the meteorites that survive transit through the atmosphere. Nevertheless, the current working assumption is that most of the extra-terrestrial material has the composition of ordinary chondrites.

As a starting point, most of the models developed for estimating the input of meteoric metals into the atmosphere assume that the relative metallic abundances in the ablated vapour are given by their meteoritic abundances (Plane, 1991; McNeil et al., 1995). The major metallic constituents by weight are then: Mg 12.5%, Fe 11.5%, Al 1.7%, Ni 1.5%, Ca 1.0%, Na 0.6% (Mason, 1971). A more realistic approach involving fractionation has been proposed recently, with the relatively volatile elements such as Na and K evaporating first and refractory elements such as Ca evaporating last (McNeil et al., 1998). This differential ablation model, which is based on fractionation models used by planetary scientists (Fegley and Cameron, 1987), was able to explain the large depletion of Ca to Na observed in meteor trails (von Zahn et al., 1999). However, it should be borne in mind that planetary fractionation models are based on equilibrium thermodynamics, whereas the average time during which a meteoroid ab-

lates is about 100 ms, so that the emergence of relatively volatile constituents may be diffusion-limited.

In this paper we describe a new Chemical Ablation Model (CAMOD), which contains the following processes: sputtering by inelastic collisions with air molecules before the meteoroid melts; evaporation of atoms and oxides from the molten particle; diffusion-controlled migration of the volatile constituents (Na and K) through the molten particle; and impact ionization of the ablated fragments by hyperthermal collisions with air molecules. The model is then used to calculate the injection rates of the more abundant elements as a function of altitude, to examine whether this accounts for the atomic Ca layer being depleted by more than two orders of magnitude compared with the Na layer (Plane, 2003). Finally, we will explore the curious finding that multiple metal resonance lidar observations of the same section of an individual meteor trail rarely observe more than one metal (von Zahn et al., 1999, 2002).

2 Model description

The architecture of CAMOD is illustrated with the flowchart in Fig. 1.

2.1 Thermal ablation

The classical theory of the interaction of meteoroids with the atmosphere has been described by a number of authors (e.g. Opik, 1958; McKinley, 1961; Evans, 1966; Hunten et al., 1980; Bronshten, 1983; Kalashnikova et al., 2000). The meteoroid is treated as a homogenous spherical particle. Radial heat transfer is assumed fast enough so the particle is isothermal along its whole path through the atmosphere (we explore this assumption below). The interaction with the atmosphere occurs in the free molecular flow regime in which the molecular collision mean free path is larger than the dimension of the meteoroid and thus no shock structure can develop. Then the loss of momentum of the particle of radius R and density ρ_m , due to interaction with the atmosphere, is

Title Page

Abstract

Introduction

Conclusions

References

Tables

Figures



Back

Close

Full Screen / Esc

Printer-friendly Version

Interactive Discussion



equal to the momentum of the impinging air molecules:

$$\frac{dV}{dt} = -\Gamma V^2 \frac{3\rho_a}{4\rho_m R} + \rho_m g \quad (1)$$

where V is the velocity of the particle, ρ_a is the mass density of the atmosphere and g the gravitational acceleration. The dimensionless “free-molecular drag” coefficient Γ expresses the efficiency of the momentum transfer between the meteoroid and impinging air molecules. Γ typically lies between 0.5 and 1 (Hughes, 1978). The gravitational term $\rho_m g$ is negligible in the range of meteoroid velocities.

The thermal energy received by the meteoroid from the impinging air molecules is balanced by radiative loss, temperature increase, melting, phase transitions, and by vaporization of the meteoric constituents (Jones and Kaiser, 1966). The energy conservation principle then gives:

$$\frac{1}{2}\pi R^2 V^3 \rho_a \Lambda = 4\pi R^2 \varepsilon \sigma (T^4 - T_{\text{env}}^4) + \frac{4}{3}\pi R^3 \rho_m C \frac{dT}{dt} + L \frac{dm}{dt} \quad (2)$$

The left-hand side of Eq. (2) represents the frictional heating term. The dimensionless parameter Λ is the “free molecular heat transfer coefficient”, which is the fraction of the incident kinetic energy which is transferred to the particle. The terms on the right-hand side of the equation represent the loss of thermal energy by the particle. The first term is the radiation loss where ε is the emissivity coefficient, σ is the Stefan-Boltzmann constant, and T and T_{env} are the temperature of the particle surface and the atmospheric environment, respectively. The second term is the heat consumed to increase the temperature of the particle (C is the bulk specific heat). The last term is the heat consumed in the transfer of particle mass into the gas phase, where L is the latent heat of vaporization (or sublimation if the particle has not melted). The emission efficiency decreases when the size of the particle is comparable to or smaller than the radiation wavelength (Bohren and Huffman, 1983). A black body at 2000 K has a peak emission wavelength of $1.45 \mu\text{m}$. Particles below this size contribute less than 10% to the total meteoroid mass entering the atmosphere, according to the LDEF

Meteoric ablation

T. Vondrak et al.

Title Page

Abstract

Introduction

Conclusions

References

Tables

Figures

◀

▶

◀

▶

Back

Close

Full Screen / Esc

Printer-friendly Version

Interactive Discussion



distribution (Love and Brownlee, 1993; McBride et al., 1999), so the size dependence of the radiative heat loss term should be negligible.

The change of particle height z with time is a function of its impact angle χ , defined as the angle to the zenith:

$$\frac{dz}{dt} = -V \cos(\chi) \quad (3)$$

The mass loss rate is calculated using Langmuir evaporation (Markova et al., 1986; Love and Brownlee, 1991; McNeil et al., 1998), which assumes that the rate of evaporation into a vacuum is equal to the rate of evaporation needed to balance the rate of uptake of a species i in a closed system. The rate of mass release of species i with molecular weight μ_i , from a particle of area S , is given by

$$\frac{dm_i^A}{dt} = \gamma \rho_i S \sqrt{\frac{\mu_i}{2\pi k_B T}} \quad (4)$$

where the superscript A refers to thermal ablation. γ is the uptake (or sticking) coefficient, equal to the probability that the molecule is retained on the surface, or within the particle, after collision. ρ_i is the thermodynamic equilibrium pressure of species i in the gas phase. The total mass loss rate due to ablation is then the sum over all gas-phase components:

$$\frac{dm^A}{dt} = \sum_i \frac{dm_i^A}{dt} \quad (5)$$

For reasons discussed below, the uptake coefficient is set to zero in the model until the temperature reaches the melting point of the particle.

2.2 Non-thermal mass loss

High velocity collisions with air molecules cause the non-thermal sputtering of atoms from the surface of the meteoroid, which results in mass loss before the particle melts

Meteoroid ablation

T. Vondrak et al.

Title Page

Abstract

Introduction

Conclusions

References

Tables

Figures

◀

▶

◀

▶

Back

Close

Full Screen / Esc

Printer-friendly Version

Interactive Discussion



Meteoric ablation

T. Vondrak et al.

Title Page

Abstract

Introduction

Conclusions

References

Tables

Figures

◀

▶

◀

▶

Back

Close

Full Screen / Esc

Printer-friendly Version

Interactive Discussion



and thermal evaporation dominates. We have therefore included a recent treatment of non-thermal interactions (Hill et al., 2005; Rogers et al., 2005), which was originally developed for gas-grain interactions in the interstellar medium (Tielens et al., 1994). The total sputtering yield at normal incidence $Y(E, \theta=0)$ per projectile of energy E (in erg), due to a cascade of binary collisions in which a fraction of recoiling surface atoms acquire energy above the surface binding forces (U_0 , in eV), is given by:

$$Y(E, \theta = 0) = 4.2 \times 10^{14} \frac{\alpha S_n(E)}{U_0} \quad (6)$$

α is a function of the mass ratio between the target and projectile, and $S_n(E)$ is the nuclear stopping cross-section (in erg cm²) which can be expressed as a function of the atomic mass and atomic number of the projectile (M_p, Z_p), and the average atomic mass and atomic number of the target (M_t, Z_t) (Sigmund, 1981):

$$S_n(E) = 4.2 \pi a Z_p Z_t e^2 \frac{M_p}{M_p + M_t} s_n(\varepsilon_{pt}) \quad (7)$$

where e is the electron charge (1 esu), and the universal function $s_n(\varepsilon_{pt})$ can be approximated as (Matsunami et al., 1980):

$$s_n(\varepsilon_{pt}) = \frac{3.411 \sqrt{\varepsilon_{pt}} \ln(\varepsilon_{pt} + 2.718)}{1 + 6.35 \sqrt{\varepsilon_{pt}} + \varepsilon_{pt} (-1.708 + 6.882 \sqrt{\varepsilon_{pt}})} \quad (8)$$

The parameter α depends on the mass ratio of target and projectile, and in the range $0.5 < M_t/M_p < 10$ can be taken as:

$$\alpha = 0.3 \left(\frac{M_t}{M_p} \right)^{\frac{2}{3}} \quad (9)$$

For a mass ratio < 0.5 , α remains approximately constant with a value around 0.2. For a mass ratio exceeding ~ 5 , Eq. (8) overestimates the multiple scattering processes.

To correct for this, α is reduced by multiplying by the ratio of the mean projected range R_{proj} to the mean penetrated path length:

$$\frac{R_{\text{proj}}}{R} = \left(K \frac{M_t}{M_p} + 1 \right)^{-1} \quad (10)$$

K depends on the material, and a value of 0.1 has been used for an iron silicate surface (Tielens et al., 1994). The screening length of the Coulomb interaction between the nuclei, a , is a function of their atomic numbers:

$$a = 0.885a_0 \left(Z_p^{2/3} + Z_t^{2/3} \right)^{-1/2} \quad (11)$$

where a_0 is the Bohr radius (in cm). The dimensionless quantity ε_{pt} is a function of the atomic masses and numbers, screening length and the projectile kinetic energy:

$$\varepsilon_{\text{pt}} = \frac{M_t}{M_p + M_t} \frac{a}{Z_p Z_t e^2} E \quad (12)$$

Sputtering can only occur if the kinetic energy of the impinging molecule overcomes the surface binding energy, U_0 . Near the threshold the ejection of the target surface atoms is due to the recoiling projectile atoms. The threshold projectile energy is then (Bohdansky et al., 1980; Anderson and Bay, 1981):

$$E_{th} = \frac{U_0}{G(1-G)} \quad \text{for } \frac{M_p}{M_t} \leq 0.3 \quad (\text{a})$$

and (13)

$$E_{th} = 8U_0 \sqrt[3]{\frac{M_p}{M_t}} \quad \text{for } \frac{M_p}{M_t} \geq 0.3 \quad (\text{b})$$



The parameter G is equal to:

$$G = \frac{4M_p M_t}{M_p + M_t} \quad (14)$$

However, over the range of meteoroid masses considered in the model (5×10^{-18} – 5×10^{-3} g), only Eq. (13a) applies. When the solution of Eq. (6) is restricted to low projectile energies ($E \ll 20 E_{th}$), where a large collision cascade is absent and only a smaller fraction of recoiling atoms has kinetic energy above U_0 , the momentum transfer is no longer isotropic. This effect is accounted for by substituting S'_n for S_n in Eq. (6) (Bohdansky et al., 1980; Yamamura et al., 1983; Bohdansky, 1984):

$$S'_n = S_n \left[1 - \left(\frac{E_{th}}{E} \right)^{\frac{2}{3}} \right] \left(1 - \frac{E_{th}}{E} \right)^2 \quad (15)$$

Based on experimental evidence the angle-averaged sputtering yield for low energy impact when the $\cos(\theta)^{-1}$ angular distribution rule holds can be taken as $\sim 2Y(E, \theta=0)$ (Draine and Salpeter, 1979). Thus for a spherical target the mass loss rate averaged over the interval 0 to $\pi/2$ is:

$$\frac{dm^s}{dt} = -2\pi R^2 V M_t \sum_i \rho_i Y_i(E, \theta=0) \quad (16)$$

where the superscript s refers to sputtering, the index i runs over all atmospheric components, ρ_i is the number density of the i -th atmospheric component, and $Y_i(E, \theta=0)$ is the sputtering cross-section for the i -th atmospheric component. The atmospheric components treated in the model are O_2 , N_2 , He, Ar, N, O and H. The sputtering cross section was assumed equal for all elements of which the target meteoroid was composed, and the elemental loss rate was derived using the bulk element atomic fractions (x_i) in the meteoroid:

$$\frac{dm_i^s}{dt} = x_i \frac{dm^s}{dt} \quad (17)$$

Meteoritic ablation

T. Vondrak et al.

Title Page

Abstract

Introduction

Conclusions

References

Tables

Figures

◀

▶

◀

▶

Back

Close

Full Screen / Esc

Printer-friendly Version

Interactive Discussion



The total mass loss rate is then the sum of the thermal ablation and sputtering rates:

$$\frac{dm}{dt} = \frac{dm^A}{dt} + \frac{dm^S}{dt} \quad (18)$$

2.3 Ionization of the ablated fragments

The ionization coefficient of an atom (or molecule) as a function of velocity, $\beta(V)$, is calculated from the expression (Jones, 1997)

$$\beta(V) = \beta_0(V) + 2 \int_{V_0}^V \beta_0(V') dV' \quad (19)$$

where

$$\beta_0 = \frac{c(V - V_0)^2 V^{0.8}}{1 + c(V - V_0)^2 V^{0.8}} \quad (20)$$

The threshold velocity V_0 is given by

$$V_0 = \sqrt{\frac{2(1 + M_e) e \phi}{M_e M_a}} \quad (21)$$

where M_e and ϕ are the mass and ionization potential of the atom (or molecule), respectively, and M_a is the average molecular mass of air. Jones does not give a value of the parameter c for Ca (Jones, 1997). We have therefore calculated β_0 for Ca using the value of c for Mg (9.29×10^{-6} Jones, 1997), but substituting the Ca ionization potential (6.113 eV Lide, 1993). The ionization coefficients of K and Na were derived by extrapolating measurements of the collisional ionization cross sections of fast alkali metal beams (Bydin and Bukhteev, 1960; Cuderman, 1972). The $\beta(V)$ dependence

Title Page

Abstract

Introduction

Conclusions

References

Tables

Figures

◀

▶

◀

▶

Back

Close

Full Screen / Esc

Printer-friendly Version

Interactive Discussion



was constructed as a least-squares fit of the experimental cross-sections to the expression:

$$\beta(V) = A (V - V_0)^2 V^B \quad (22)$$

where $A=0.933$ and $B=-1.94$ for Na, and $A=0.347$ and $B=-1.702$ for K. The extrapolated ionization coefficients and experimental values for the alkali metals are shown in Fig. 2 together with the experimental values. The β values for other metals derived from Eq. (19) are included for comparison.

2.4 Diffusion-controlled ablation of alkali metals

The relative abundances of sodium and potassium in chondritic meteorites are 0.80 and 0.051 atomic%, respectively (Mason, 1971; Fegley and Cameron, 1987; Lodders and Fegley, 1988; Sears and Dodd, 1988). Therefore, the evaporation of these elements from the meteoroid does not change the size of the particle nor affect its temperature significantly. Thus the temperature of the particle derived from Eq. (2) can be used to estimate the diffusion coefficient, $D(T)$, of the alkali metals in the molten meteoroid. The temperature dependence of $D(T)$ is given approximately (ignoring the activation volume) by:

$$D(T) = D_0 \exp(E_A/RT) \quad (23)$$

where D_0 is $1.48 \times 10^{-5} \text{ m}^2 \text{ s}^{-1}$ for K and $9.84 \times 10^{-5} \text{ m}^2 \text{ s}^{-1}$ for Na (Sigurdsson et al., 2000). The activation energy (E_A) for K does not seem to have been reported, and so we have adopted for K the value for Na (167 kJ mol^{-1}). The fraction of a species diffusing from a spherical particle in the time interval Δt is given by (Crank, 1975):

$$f(\Delta t, T) = \frac{6}{\pi^2} \sum_{n=1}^{\infty} \frac{1}{n^2} \exp(-D(T) n^2 \pi^2 \Delta t / r^2) \quad (24)$$

Equation (24) was solved with a vertical resolution of 100 m; Δt is then the time the particle travelled each 100 m step, within which T was held constant.

Title Page

Abstract

Introduction

Conclusions

References

Tables

Figures

◀

▶

◀

▶

Back

Close

Full Screen / Esc

Printer-friendly Version

Interactive Discussion



2.5 Vapour – molten meteoroid thermodynamic equilibrium

The vapour pressures of the species evaporating from the meteoroid were calculated using the MAGMA chemical equilibrium code (Fegley and Cameron, 1987; Schaefer and Fegley, 2004, 2005). The code is robust and fast, and exhibits good agreement with experimental data for a wide range of temperatures and silicate melt compositions. MAGMA uses the ideal mixing of complex components modelled by Hastie and coworkers (Hastie et al., 1982a, 1982b, 1984; Hastie and Bonnell, 1985, 1986), and takes account of the equilibria of eight metal oxides: SiO₂, MgO, FeO, Al₂O₃, TiO₂, CaO, Na₂O and K₂O. The chemical equilibria in the melts are modelled using thermodynamic activities, a_j , which are given by

$$a_j = \gamma_j X_j \quad (25)$$

where X_j is the mole fraction of oxide in the melt and γ_j is the Raoultian activity coefficient of the oxide relative to the pure liquid oxide. The melt is then modelled as a non-ideal solution in which the concentrations of the unbound metal oxides are reduced by the formation of complex oxides and pseudo-components. The activities of the oxides in the non-ideal melts are calculated from the mole fractions of the unbound oxides in the melt, i.e.

$$a_{\text{oxide}} = X_{\text{oxide}}^* \quad (26)$$

where X_{oxide}^* is the mole fraction of the unbound oxide in the melt. The equilibria between components in the melt, and between the melt and vapour, are calculated simultaneously. It is assumed that the oxides evaporate stoichiometrically. The vapour pressure of each gas-phase species is then used to determine the mass loss rate of that component from the melt by invoking Langmuir evaporation (Eq. 4).

2.6 Integration and the initial distribution of the meteoroids

A fourth-order Runge-Kutta numerical integration scheme with adaptive step size control (Press et al., 1992) is used to integrate the above sets of differential equations

Title Page

Abstract

Introduction

Conclusions

References

Tables

Figures

◀

▶

◀

▶

Back

Close

Full Screen / Esc

Printer-friendly Version

Interactive Discussion



Meteoric ablation

T. Vondrak et al.

[Title Page](#)[Abstract](#)[Introduction](#)[Conclusions](#)[References](#)[Tables](#)[Figures](#)[◀](#)[▶](#)[◀](#)[▶](#)[Back](#)[Close](#)[Full Screen / Esc](#)[Printer-friendly Version](#)[Interactive Discussion](#)

(Eqs. 1–5, and 16–18). As shown in Fig. 1, the integration starts at an altitude of 500 km and meteoroid temperature of 200 K. After the particle has started to heat, the integration is stopped if the meteoroid mass decreases below 10^{-26} g or the meteoroid temperature falls below 400 K. Otherwise the integration continues until the final altitude of 40 km. The resulting masses, ablation rates and temperature are then interpolated onto a regularly spaced 100 m step altitude grid.

The model input parameters are listed in Table 1. The meteoroid mass and velocity distributions from the LDEF satellite experiment (Love and Brownlee, 1993; McBride et al., 1999) were used. The mass distribution in the model is from 5×10^{-18} g to 5×10^{-3} g. Larger particles would not fulfil the isothermicity condition (see Sect. 3.1 below). However, since particles heavier than 5×10^{-3} g contribute less than 9% to the total input mass, imposing this upper limit will not significantly affect the calculated total mass released into the Earth's atmosphere. The extraterrestrial material is assumed to have a CI chondrite composition, with elemental abundances in Table 2 that are taken from three sources (Mason, 1971; Lodders and Fegley, 1988; Sears and Dodd, 1988).

3 Results and discussion

All the results presented here are for the conditions of March at 40° N. The number densities of atmospheric constituents were calculated using the MSISE-90 model for 2001 (Hedin et al., 1991). In the following discussion, the “most probable” meteoroid refers to a particle of mass $5 \mu\text{g}$ (the most probable size in the LDEF size distribution (McBride et al., 1999)) and density 2 g cm^{-3} . All model runs employed an entry angle $\theta=37^\circ$ (Hunten et al., 1980), unless otherwise stated.

3.1 Heat transport in the meteoric particle

The application of the thermodynamic equilibrium model requires a uniform temperature across the meteoroid. If the particle is not isothermal the composition and chemi-

cal states of elements would differ between the skin and inner region of the particle. In these circumstances the MAGMA code would not provide the correct vapour pressures of the gas-phase species from the bulk composition of the particle. The isothermal condition can be assessed by the dimensionless Biot number. For a spherical object the

5 Biot number is given by

$$Bi = \frac{hR}{3k} \quad (27)$$

where h is the heat transfer coefficient ($W m^{-2} K^{-1}$), R is the radius and k the thermal conductivity ($W m^{-1} K^{-1}$). If $Bi < 0.1$, the object can be considered isothermal (Kakac and Yener, 1985). If non-radiative heat losses from the particle are omitted, the heat transfer coefficient can be expressed as (Love and Brownlee, 1991):

10

$$h = \sigma T^3 \quad (28)$$

Figure 3 shows the calculated Bi for a range of initial particle masses over the temperature range in which the meteoroid ablates, using a thermal conductivity for olivine rock of $1 W m^{-1} K^{-1}$ (Buttner et al., 1998). This shows that the most probable $5 \mu g$ particle is isothermal up to a very high temperature, and the largest mass used in the model stays isothermal up to $\sim 2500 K$ if the density is $2 g cm^{-3}$. Because meteoroids lose mass extensively above $\sim 2800 K$ they become much smaller at the highest temperatures attained, reducing Bi further. Thus the isothermicity condition seems fulfilled for the whole mass distribution up to $5 \times 10^{-3} g$.

15

20

3.2 Melting of the meteoroid

The MAGMA code gives non-zero vapour pressures for metal species at temperatures below the melting temperature of the meteoroid. However, thermodynamic equilibrium in the meteoroid cannot be established before the particle melts. Thus the melting temperature has to be entered as an external parameter into the integration procedure. Mineralogically, CI chondrites have an olivine composition (Mason, 1971; Lodders and Fegley, 1988; Sears and Dodd, 1988). The olivine phase diagram shows that

25

Meteoric ablation

T. Vondrak et al.

Title Page

Abstract

Introduction

Conclusions

References

Tables

Figures

◀

▶

◀

▶

Back

Close

Full Screen / Esc

Printer-friendly Version

Interactive Discussion



Meteoric ablation

T. Vondrak et al.

[Title Page](#)[Abstract](#)[Introduction](#)[Conclusions](#)[References](#)[Tables](#)[Figures](#)[◀](#)[▶](#)[◀](#)[▶](#)[Back](#)[Close](#)[Full Screen / Esc](#)[Printer-friendly Version](#)[Interactive Discussion](#)

for the chondritic Fe/Mg ratio of ~ 0.8 , olivine starts to melt at 1730 K (Fig. 4a). The onset of particle evaporation in CAMOD is simulated by applying a sigmoid temperature dependence to the uptake coefficient γ in Eq. (4). A finite smooth melting range describes in a more realistic way the phase change than an instantaneous transition to the molten state at the threshold temperature, and also prevents instability in the numerical integration. In practice, the value of the melting temperature only affects the altitude of the deposition of the alkali metals: within the temperature range which encompasses the olivine phase equilibrium (1600–2000 K), the altitude of the Na ablation peak varies from 96–101 km (Fig. 4b). We have adopted a meteoroid melting temperature of 1800 K, and γ varies from 0 ($T < 1700$ K) to 1 ($T > 1900$ K) for all the model runs discussed below. The meteoroid mass-velocity combinations which undergo thermal ablation are shown in Fig. 5, for a range of particle densities ($0.3\text{--}3\text{ g cm}^{-3}$). This demonstrates that the velocity at which the particle temperature reaches the ablation threshold is a steep function of particle density.

Figure 6 shows the dependence with entry velocity of the height at which meteoroids (mass range $0.05\text{--}500\ \mu\text{g}$) are predicted to melt. The modelled dependence is compared with the appearance height of meteor head echoes observed by the 430 MHz Arecibo incoherent radar (Janches and ReVelle, 2005). Note that the velocity measured by the radar is the vertical component, along the line-of-sight of the radar. There is very good agreement for velocities between 20 km s^{-1} and 45 km s^{-1} . At velocities below 20 km s^{-1} the head echoes appear 10–15 km higher. However, this discrepancy is most probably explained by meteoroids crossing the radar beam at large entry angles, and thus with small measured vertical velocity components. Indeed, this must explain the velocities below 11 km s^{-1} observed by the radar.

At velocities above 45 km s^{-1} , the model predicts much higher appearance heights for smaller meteoroids than the average appearance heights of the Arecibo observations. There are two likely reasons for this. First, immediately after the particle melts, the volatile elements Na and K ablate (see Figs. 8 and 10 below). Although these elements ionize efficiently at high impact velocities (see Fig. 14 below), they comprise

Meteoric ablation

T. Vondrak et al.

[Title Page](#)[Abstract](#)[Introduction](#)[Conclusions](#)[References](#)[Tables](#)[Figures](#)[◀](#)[▶](#)[◀](#)[▶](#)[Back](#)[Close](#)[Full Screen / Esc](#)[Printer-friendly Version](#)[Interactive Discussion](#)

less than 1% of the meteoroid mass and so the rate of electron production contributing to the meteor head echo is small. In contrast, the bulk constituents (Fe, Mg and Si) ablate about 10 km lower (Fig. 10, below), when the rate of electron production will be considerably higher. Second, the head echo is proportional to the square root of the electron density around the meteoroid, and the electron density in turn varies inversely with atmospheric density because the electron cloud expands to about one mean free path around the meteoroid (Dyrud et al., 2005). The head echo thus drops by ~ 10 dB for a 10 km height increase. Note that even though these two factors mitigate against observing small high velocity meteoroids at the altitudes where thermal ablation begins, the Arecibo radar does in fact see a small number of particles above 120 km (Janches et al., 2003). The coupling of CAMOD with a meteor head echo model will be used for exploring these effects in a future study.

3.3 Non-thermal mass loss

Sputtering as a parallel mechanism to thermal ablation was first proposed by Öpik (1958), and is the main mass loss mechanism for particles which do not melt (e.g. Lebedinets and Shushkova, 1970a, 1970b). More recently, a simple sputtering mechanism was incorporated into a meteor model (Coulson, 2002; Coulson and Wickramasinghe, 2003), followed by a more detailed sputtering model which included the variation of atmosphere composition along the meteoroid trajectory (Rogers et al., 2005).

The fraction of mass loss before the meteoroid reaches 1700 K and thermal ablation starts is shown in Fig. 7, over the range of meteoroid masses and entry velocities. Clearly the effect of sputtering is negligible for meteoroids with velocities up to 45 km s^{-1} and heavier than 10^{-11} g . Only the fastest particles up to masses of 10^{-14} g are reduced to approximately half of their initial mass by sputtering.

3.4 Diffusion-controlled ablation of Na and K

The alkali elements are the most volatile metallic constituents of meteoroids and, according to the thermodynamic model with Langmuir evaporation, should ablate very quickly after the meteoroid melts. This raises the question of whether the rate of ablation of Na (and K) could in fact be kinetically controlled by diffusion out of the molten particle. Figure 8 shows the altitude profiles of Na ablating from the most probable meteoroid for a range of entry velocities, when evaporation is controlled either by diffusion (Eqs. 23 and 24) or by Langmuir evaporation (Eq. 4). Inspection of this figure demonstrates that for slow meteoroids (V up to $\sim 20 \text{ km s}^{-1}$) the ablation profiles are similar: the FWHMs (full-width-at-half-maximum) of the ablation profiles differ by less than 50%. In contrast, radial diffusion significantly broadens (by a factor of ~ 2.5) the ablation profile of the fastest meteoroid at 72 km s^{-1} . However, the weighting of the fast particles in the meteoroid velocity distribution (Love and Brownlee, 1993; McBride et al., 1999) is a few orders of magnitude lower than the weighting of the most probable V ($\sim 20 \text{ km s}^{-1}$). Thus, the total injection profiles of the alkali metals, obtained by summing over the whole meteoroid velocity and mass distribution (Sect. 3.5), is hardly affected by including diffusion control.

3.5 Elemental ablation profiles in the atmosphere

The fraction of a meteoroid that ablates is shown as a function of mass and entry velocity in Fig. 9. The lower mass threshold for complete evaporation of the fastest meteoroid particles is $\sim 10^{-10} \text{ g}$. The mass threshold for nearly complete (95%) ablation as a function of meteoroid velocity can be expressed by the following inequality ($\rho_m = 2 \text{ g cm}^{-3}$):

$$\log_{10}(\text{mass in g}) \geq 4.47766 - 0.64892 V + 0.01102 V^2 - 6.96685 \times 10^{-5} V^3 \quad (29)$$

where V is the meteoroid velocity in km s^{-1} .

Title Page

Abstract

Introduction

Conclusions

References

Tables

Figures

◀

▶

◀

▶

Back

Close

Full Screen / Esc

Printer-friendly Version

Interactive Discussion



Meteoric ablation

T. Vondrak et al.

[Title Page](#)[Abstract](#)[Introduction](#)[Conclusions](#)[References](#)[Tables](#)[Figures](#)[◀](#)[▶](#)[◀](#)[▶](#)[Back](#)[Close](#)[Full Screen / Esc](#)[Printer-friendly Version](#)[Interactive Discussion](#)

The elemental deposition profiles for the most probable meteoroid are shown in Fig. 10. Na and K are released at ~ 99 km; their vaporization is almost complete before other elements start to evaporate. Indeed, the less volatile major components Si, Fe and Mg are released 10–15 km lower in the atmosphere. The ablation of Na, K, Fe, Si, and Mg is nearly complete and thus the relative abundance of these elements in the gas phase is very similar to the meteoroid before entry. The behaviour of Ca is strikingly different: less than 1% of this element is released from the particle. The Na/Ca ratio in the gas phase is thus ~ 170 times larger than in the meteoroid. Interestingly, this ratio is similar to the ratio of the column densities of the background Na and Ca layer observed by lidar (Qian and Gardner, 1995).

In contrast, the integration of the elemental ablation profiles over the meteoroid velocity and mass distributions, to yield the total injection rate of each element, presents a somewhat different picture. Figure 11 shows that the peak release of the alkali metals remains approximately 10 km above the major meteoric components, but the Na/Ca ratio is now only 4:1. This arises because the fraction of Ca that ablates is strongly dependent on entry velocity. As shown in Fig. 12 (middle panel), Ca is not released from the most probable meteoroid until V exceeds 20 km s^{-1} . At higher velocities, the fraction of ablated Ca increases steeply to reach 1.0 at $V = 35 \text{ km s}^{-1}$.

The threshold velocity for Ca ablation and the velocity at which complete ablation of Ca occurs also depend strongly on the meteoroid mass, as shown in the three panels of Fig. 12. A $50 \mu\text{g}$ particle has an ablation threshold velocity of only 15 km s^{-1} and the Ca ablates completely above 30 km s^{-1} , whereas for a $0.05 \mu\text{g}$ particle these velocities are 35 and 55 km s^{-1} , respectively. Indeed, simultaneous common-volume lidar measurements of Ca and Fe have shown that the Ca/Fe ratio in fresh meteor trails approaches the chondritic ratio as the meteoroids get larger (von Zahn et al., 2002). These model predictions are also in accord with steady-state evaporation experiments using FeO–MgO–SiO₂–CaO–Al₂O₃ chondritic melts (Hashimoto et al., 1979; Hashimoto, 1983). The first stage of heating is associated with the loss of FeO, and a significant enrichment of CaO and Al₂O₃ occurs after 70% of the mass has evaporated.

Lastly, cosmic spherules that exhibit progressive heating are characterized by loss of the more volatile oxides and become Ca-Al-Ti-rich (Taylor et al., 2000).

The injection rate profiles plotted in Fig. 11 are the current best estimates for use in atmospheric models of the mesospheric metal layers. Note that these injection rates should be scaled by a factor of 0.34 if the total mass flux is around 30 t d^{-1} , as argued in Sect. 1. Future refinements to this average picture can be made by applying CAMOD to the seasonal and latitudinal variations of the meteoroid mass, velocity and entry angle distributions, as well as considering different compositions for meteoroids depending on their origin (Janches et al., 2006; Fentzke and Janches, 2008).

3.6 Lidar detection of K, Ca and Ca^+ in meteor trails

One test of CAMOD is to explain the finding that when common-volume lidar measurements are made of two or three metals, meteor trails that pass through the common volume rarely contain more than a single metal: two metals are seen <1% of the time, and three metals only once out of thousands of observed trails (von Zahn et al., 2002).

Here we focus on simultaneous common-volume lidar measurements of K and Ca performed during a meteor shower (Gerding et al., 1999). Because the lidar beams were zenith-pointing, and meteor trails are typically inclined at an angle to the zenith, the lidars would only have observed at most a few 100 m along the trail. The most striking feature of the observations of ~ 30 meteor trails was an absence of a simultaneous detection of the two elements, and a preponderance (>80%) of Ca-containing trails within a height range of 92–95 km. CAMOD predicts that a $50 \mu\text{g}$ meteoroid (i.e. large enough to release a measurable amount of Ca) will inject Ca at these altitudes if the entry velocity is $\sim 50 \text{ km s}^{-1}$ (Fig. 13, left-hand panel). In contrast, K will then ablate at an altitude of $\sim 112 \text{ km}$ if Langmuir evaporation is rate-limiting, or $\sim 109 \text{ km}$ when diffusion out of the meteoroid is rate-limiting. However, above 100 km the probability of detecting K in the trail is strongly reduced because of the rapid expansion of the trail by radial diffusion at the lower atmospheric pressure (Höffner et al., 1999). Furthermore, Fig. 14 shows that most of the potassium ($\sim 80\%$) will be ionized by hyperthermal colli-

Title Page

Abstract

Introduction

Conclusions

References

Tables

Figures

◀

▶

◀

▶

Back

Close

Full Screen / Esc

Printer-friendly Version

Interactive Discussion



sions at this entry velocity, whereas a much smaller fraction ($\sim 25\%$) of calcium will be ionized.

To release K around 90 km, where K trails have been observed (Gerding et al., 1999), the initial velocity of the meteoroid must be around 12 km s^{-1} (Fig. 13, right-hand panel). At this low velocity only $\sim 10\%$ of the ablating K will undergo collisional ionization (Fig. 14). However, the peak temperature reached by the meteoroid is only $\sim 2300 \text{ K}$, and so only a trace ($< 0.1\%$) of Ca ablates (Fig. 13, right panel). Thus, CAMOD is able to explain the presence of either K or Ca, but not both metals, in simultaneous lidar observations of the same section of a meteor trail.

Von Zahn et al. (2002) have reported simultaneous common-volume measurements of Ca and Ca^+ in meteor trails, using the resonance lidar technique (Alpers et al., 1996). The mean height at which these layers were observed was 94.5 km, and the Ca^+/Ca ratio was greater than 1. As shown in Fig. 14, a 50% ionization rate of Ca is only reached for impact velocities of $\sim 70 \text{ km s}^{-1}$, and it is very unlikely that all the trails observed by von Zahn et al. (2002) were produced by such high speed meteoroids (indeed, the left-hand panel of Fig. 13 indicates that an entry velocity around 50 km s^{-1} should produce a Ca trail at 95 km). This discrepancy probably indicates that our estimate of the collisional ionization efficiency of Ca, made using a semi-empirical formalism (Eqs. 19–21, Jones, 1997), underestimates β by a factor of 2–3.

3.7 Differential ablation of Ca – sensitivity to model parameters

The model results presented in Tables 3 and 4 were obtained assuming a bulk meteoroid density of 2 g cm^{-3} and heat of vaporization of 6 MJ kg^{-1} . Although a density of 2 g cm^{-3} was assumed for analysis of the LDEF cratering experiment (Love et al., 1995), the bulk porosity of incoming extraterrestrial particles is rather uncertain (Love et al., 1993; 1994; Rietmeijer, 2002). We now consider a series of densities in the range 0.3 to 3.5 g cm^{-3} . The lowest density is typical of highly porous extraterrestrial material of cometary origin, whereas asteroidal material is thought to have a density of $\sim 3 \text{ g cm}^{-3}$ (Rietmeijer, 2002). For comparison, the density of olivine lies between

Meteoric ablation

T. Vondrak et al.

Title Page

Abstract

Introduction

Conclusions

References

Tables

Figures

◀

▶

◀

▶

Back

Close

Full Screen / Esc

Printer-friendly Version

Interactive Discussion



3.2 g cm⁻³ (forsterite) and 4.3 g cm⁻³ (fayalite) (Lide, 1993).

Figure 15 shows the effect of the meteoroid density on the ablated fraction of each element and the centroid height of its ablation profile, integrated over the LDEF particle mass and velocity distributions. When the density increases from 0.3 to 3.5 g cm⁻³ (the mass distribution is conserved, so the particle volume decreases as ρ_m^{-1}), the total ablated fraction increases nearly 2-fold. However, the increases of the individual elements vary from 1.3 (Na, K) to 2.4 (Ca). The centroid heights of the elemental ablation profiles decrease by 3.6 km (Na, K) to 7.1 km (Ca). Thus the relative amount of ablated Ca changes by less than a factor of 2 for a 10-fold increase of ρ_m . This indicates that a meteoroid population with a density very different from 2 g cm⁻³ is unlikely to explain the depletion of atomic Ca, relative to Na and Fe, in the upper mesosphere.

Vaporization of the meteoroid is the main cooling mechanism once the particle has melted. In spite of this, the effect of halving the heat of vaporization, L , brings about a less than 5% increase of the deposited metals and a negligible shift of the injection profile peaks (Table 5). The ablation efficiency is also not sensitive to the specific heat of the meteoroid, C . For example, increasing C by a factor of 3 causes less than 1% change in the total ablated fraction, and shifts the ablation centroid heights less than 1 km.

Lastly we consider the meteoroid incidence angle χ . Table 4 shows that the injection rates of the major components and alkali metals are only slightly larger (<10%) for zenith incidence compared to $\chi=37^\circ$, although the refractive metals (Ca, Ti, and Al) show more sensitivity to χ : their integrated injection rates increase by 13–20%. The centroid heights of the injection profiles shift down between 0.1 and 3 km at $\chi=0^\circ$.

4 Conclusions

A model of the chemical ablation of meteoroids in the upper atmosphere has been described. Na and K evaporate first, several km above the main constituents Fe, Mg and

Meteoroid ablation

T. Vondrak et al.

Title Page

Abstract

Introduction

Conclusions

References

Tables

Figures

◀

▶

◀

▶

Back

Close

Full Screen / Esc

Printer-friendly Version

Interactive Discussion



Meteoric ablation

T. Vondrak et al.

[Title Page](#)[Abstract](#)[Introduction](#)[Conclusions](#)[References](#)[Tables](#)[Figures](#)[◀](#)[▶](#)[◀](#)[▶](#)[Back](#)[Close](#)[Full Screen / Esc](#)[Printer-friendly Version](#)[Interactive Discussion](#)

Si. CAMOD successfully predicts over a broad of meteoroid velocities the meteor head echo appearance heights measured by incoherent scatter radar, although the discrepancy noted at the highest velocities will be the subject of future work where CAMOD is coupled to a head echo model. CAMOD also explains common-volume lidar observations of K, Ca and Ca⁺ in fresh meteor trails. The ablation of Ca relative to the major constituents and alkalis depends strongly on the initial velocity of meteoroids. The Na:Ca ratio of 100–360 observed in the metal atom layers in the upper mesosphere is reproduced only for slow meteoroids (velocity <20 km s⁻¹). However, CAMOD predicts a ratio of only 4:1 integrated over the commonly assumed distribution of meteoroid mass and velocity. This result is also not very sensitive to the meteoroid density, heat of evaporation, and angle of entry assumed in the model. The explanation for the more than 2 orders of magnitude depletion of Ca relative to Na atoms in the mesosphere, compared with their chondritic abundance (~1:1), must therefore lie elsewhere.

Acknowledgements. This work and a studentship for SLB was supported by NERC grant NE/B00015X/1. TV was partially supported by a fellowship from the University of Leeds. DJ was supported under NSF Grant ATM-05311464 and agreement 51861-8406 between Cornell University and NWRA. The Arecibo Observatory is part of the National Astronomy and Ionosphere Center, which is operated by Cornell University under cooperative agreement with the NSF.

References

Alpers, M., Höffner, J., and von Zahn, U.: Upper Atmosphere Ca and Ca⁺ at Mid-Latitudes: First Simultaneous and Common-Volume Lidar Observations, *Geophys. Res. Lett.*, 23, 567–570, 1996.

Anderson, H. H. and Bay, H. L.: Sputtering yield measurements, Springer-Verlag, Berlin, 145–218, 1981.

Baggaley, W. J.: Radar observations, in: *Meteors in the Earth's Atmosphere*, edited by: E. Murad and I. P. Williams, 123–148, Cambridge University press, Cambridge, 2002.

Meteoric ablation

T. Vondrak et al.

Title Page

Abstract

Introduction

Conclusions

References

Tables

Figures

◀

▶

◀

▶

Back

Close

Full Screen / Esc

Printer-friendly Version

Interactive Discussion



Bohdansky, J.: A Universal Relation for the Sputtering Yield of Monatomic Solids at Normal Ion Incidence, *Nuclear Instruments & Methods in Physics Research Section B-Beam Interactions with Materials and Atoms*, 230, 587–591, 1984.

Bohdansky, J., Roth, J., and Bay, H. L.: An Analytical Formula and Important Parameters for Low-Energy Ion Sputtering, *J. Appl. Phys.*, 51, 2861–2865, 1980.

Bohren, C. F. and Huffman, D. R.: *Absorption and Scattering of Light by Small Particles*, Wiley-Interscience, New York, 130–157, 1983.

Bronshthen, V. A.: *Physics of Meteoric Phenomena*, Reidel, New York, 356 pp., 1983.

Buttner, R., Zimanowski, B., Blumm, J., and Hagemann, L.: Thermal conductivity of a volcanic rock material (olivine-melilitite) in the temperature range between 288 and 1470 K, *J. Volcan. Geotherm. Res.*, 80, 293–302, 1998.

Bydin, Y. F. and Bukhteev, A. M.: Ionization of Fast Na, K, Rb, and Cs Atoms in Collisions with H₂, D₂, N₂, and O₂ Molecules, *Sov. Phys.-Tech. Phys.*, 5, 512–519, 1960.

Ceplecha, Z., Borovicka, J., Elford, W. G., Revelle, D. O., Hawkes, R. L., Porubcan, V., and Simek, M.: Meteor phenomena and bodies, *Space Sci. Rev.*, 84, 327–471, 1998.

Close, S., Hunt, S., Minardi, M., and McKeen, F.: Analysis of Perseid meteor head echo data collected using the ALTAIR radar, *Radio Sci.*, 35, 1233–1240, 2000.

Coulson, S. G.: Resistance of motion to a small, hypervelocity sphere, sputtering through a gas, *Monthly Notices of the Royal Astronomical Society*, 332, 741–744, 2002.

Coulson, S. G. and Wickramasinghe, N. C.: Frictional and radiation heating of micron-sized meteoroids in the Earth's upper atmosphere, *Mon. Not. R. Astron. Soc.*, 343, 1123–1130, 2003.

Crank, J.: *The mathematics of diffusion*, 2nd ed., Oxford University Press, Oxford, 84–87, 1975.

Cuderman, J. F.: Ionization of K-Atoms in Collision with H₂, N₂, O₂, and CO, *Phys. Rev. A*, 5, 1687–1692, 1972.

Curtius, J., Weigel, R., Vossing, H. J., Wernli, H., Werner, A., Volk, C. M., Konopka, P., Krebsbach, M., Schiller, C., Roiger, A., Schlager, H., Dreiling, V., and Borrmann, S.: Observations of meteoric material and implications for aerosol nucleation in the winter Arctic lower stratosphere derived from in situ particle measurements, *Atmos. Chem. Phys.*, 5, 3053–3069, 2005,

<http://www.atmos-chem-phys.net/5/3053/2005/>.

Cziczo, D. J., Thomson, D. S., and Murphy, D. M.: Ablation, flux, and atmospheric implications

- of meteors inferred from stratospheric aerosol, *Science*, 291, 1772–1775, 2001.
- Draine, B. T. and Salpeter, E. E.: Physics of Dust Grains in Hot Gas, *Astrophys. J.*, 231, 77–94, 1979.
- Dyrud, L. P., Denney, K., Urbina, J., Janches, D., Kudeki, E., and Franke, S.: The meteor flux: It depends how you look, *Earth Moon Planets*, 95, 89–100, 2005.
- Evans, J. V.: Radar Observation of Meteor Deceleration, *J. Geophys. Res.*, 71, 171–188, 1966.
- Fegley, B. and Cameron, A. G. W.: A Vaporization Model for Iron Silicate Fractionation in the Mercury Protoplanet, *Earth Planet. Sci. Lett.*, 82, 207–222, 1987.
- Fentzke, J. T. and Janches, D.: A semi-empirical model of the contribution from sporadic meteoroid sources on the meteor input function in the MLT observed at Arecibo, *J. Geophys. Res.*, 113, Article Number-A03304, 2008.
- Gabrielli, P., Barbante, C., Plane, J. M. C., Varga, A., Hong, S., Cozzi, G., Gaspari, V., Planchon, F. A. M., Cairns, W., Ferrari, C., Crutzen, P., Cescon, P., and Boutron, C. F.: Meteoric smoke fallout over the Holocene epoch revealed by iridium and platinum in Greenland ice, *Nature*, 432, 1011–1014, 2004.
- Gerding, M., Alpers, M., Höffner, J., and von Zahn, U.: Simultaneous K and Ca lidar observations during a meteor shower on March 6–7, 1997, at Klungsborn, Germany., *J. Geophys. Res.*, 104, 24 689–24 698, 1999.
- Hashimoto, A.: Evaporation metamorphism in the early solar nebula-evaporation experiments on the melt FeO-MgO–SiO₂-CaO-Al₂O₃, *Geochem. J.*, 17, 111–145, 1983.
- Hashimoto, A., Kumazawa, M., and Oniima, N.: Evaporation metamorphism of primitive dust material in the early solar nebula, *Earth Planet. Sci. Lett.*, 43, 13–21, 1979.
- Hastie, J. W. and Bonnell, D. W.: A Predictive Phase-Equilibrium Model for Multicomponent Oxide Mixtures .2. Oxides of Na-K-Ca-Mg-Al-Si, *High Temp. Sci.*, 19, 275–306, 1985.
- Hastie, J. W. and Bonnell, D. W.: A Predictive Thermodynamic Model of Oxide and Halide Glass Phase-Equilibria, *J. Non-Crystalline Solids*, 84, 151–158, 1986.
- Hastie, J. W., Bonnell, D. W., Plante, E. R., and Horton, W. S.: Thermodynamic activity and vapor pressure models for silicate systems including coal slags, in: *Thermochemistry and its Application to Chemical and Biochemical Systems*, edited by: Ribeiro da Silva, M. A. V., 235–251, Reidel, Dordrecht, 1984.
- Hastie, J. W., Horton, W. S., Plante, E. R., and Bonnell, D. W.: Thermodynamics Models of alkali-metal vapor transport in silicate systems, *High Temp.-High Press.*, 14, 669–679, 1982a.

Meteoric ablation

T. Vondrak et al.

[Title Page](#)[Abstract](#)[Introduction](#)[Conclusions](#)[References](#)[Tables](#)[Figures](#)[◀](#)[▶](#)[◀](#)[▶](#)[Back](#)[Close](#)[Full Screen / Esc](#)[Printer-friendly Version](#)[Interactive Discussion](#)

Meteoric ablation

T. Vondrak et al.

[Title Page](#)[Abstract](#)[Introduction](#)[Conclusions](#)[References](#)[Tables](#)[Figures](#)[◀](#)[▶](#)[◀](#)[▶](#)[Back](#)[Close](#)[Full Screen / Esc](#)[Printer-friendly Version](#)[Interactive Discussion](#)

- Hastie, J. W., Plante, E. R., and Bonnell, D. W.: Alkali vapor transport in coal convesion and combustion systems, in *Metal Bonding and Interaction in High Temperature Systems*, edited by: Gole, J. L. and Stwalley, W. C., pp. 543–600, Am. Chem. Soc., Washington, D.C., 1982b.
- Hedin, A. E., Biondi, M. A., Burnside, R. G., Hernandez, G., Johnson, R. M., Killeen, T. L.,
5 Mazaudier, C., Meriwether, J. W., Salah, J. E., Sica, R. J., Smith, R. W., Spencer, N. W., Wickwar, V. B., and Viridi, T. S.: Revised Global-Model of Thermosphere Winds Using Satellite and Ground-Based Observations, *J. Geophys. Res.*, 96, 7657–7688, 1991.
- Hill, K. A., Rogers, L. A., and Hawkes, R. L.: Sputtering and high altitude meteors, *Earth Moon Planets*, 95, 403–412, 2005.
- 10 Höffner, J., von Zahn, U., McNeil, W. J., and Murad, E.: The 1996 Leonid shower as studied by potassium lidar, *J. Geophys. Res.*, 104, 2633–2643, 1999.
- Hughes, D. W.: *Meteors*, in *Cosmic Dust*, edited by: J. A. M. McDonnell, 123–185, Wiley, London, 1978.
- Hughes, D. W.: *Meteors and cosmic dust*, *Endeavour*, 21, 31–35, 1997.
- 15 Hunten, D. M., Turco, R. P., and Toon, O. B.: Smoke and Dust Particles of Meteoric Origin in the Mesosphere and Stratosphere, *J. Atmos. Sci.*, 37, 1342–1357, 1980.
- Janches, D., Close, S., and Fentzke, J. T.: A comparison of detection sensitivity between ALTAIR and Arecibo meteor Observations: Can High Power and Large Aperture radars detect low velocity meteor head echoes?, *Icarus*, 193, 105–111, 2007.
- 20 Janches, D., Heinselman, C. J., Chau, J. L., Chandran, A., and Woodman, R.: Modeling the global micrometeor input function in the upper atmosphere observed by high power and large aperture radars, *J. Geophys. Res.*, 111, Article Number A07317, 2006.
- Janches, D., Mathews, J. D., Meisel, D. D., and Zhou, Q. H.: Micrometeor observations using the Arecibo 430 MHz radar I. Determination of the ballistic parameter from measured Doppler
25 velocity and deceleration results, *Icarus*, 145, 53–63, 2000.
- Janches, D., Nolan, M. C., Meisel, D. D., Mathews, J. D., Zhou, Q. H., and Moser, D. E.: On the geocentric micrometeor velocity distribution, *J. Geophys. Res.*, 108, 1222, 2003.
- Janches, D. and ReVelle, D. O.: Initial altitude of the micrometeor phenomenon: Comparison between Arecibo radar observations and theory, *J. Geophys. Res.*, 110, A08307, 2005.
- 30 Jones, J. and Kaiser, T. R.: The effects of thermal radiation, conduction, and meteoroid heat capacity on meteoroid ablation, *Mon. Not. R. Astron. Soc.*, 133, 411–420, 1966.
- Jones, W.: Theoretical and observational determinations of the ionization coefficient of meteors, *Mon. Not. R. Astron. Soc.*, 288, 995–1003, 1997.

- Kakac, S. and Yener, Y.: Heat conduction, Hemisphere, New York, 15 pp., 1985.
- Kalashnikova, O., Horanyi, M., Thomas, G. E., and Toon, O. B.: Meteoric Smoke production in the atmosphere, *Geophys. Res. Lett.*, 27, 3293–3296, 2000.
- Lanci, L., Kent, D. V., and Biscaye, P. E.: Meteoric smoke concentration in the Vostok ice core estimated from superparamagnetic relaxation and some consequences for estimates of Earth accretion rate, *Geophys. Res. Lett.*, 34, L10803, doi:10.1029/2007GL029811, L10803, 2007.
- Lebedinets, V. N. and Shushkova, V. B.: Meteor Ionisation in E-Layer, *Planet. Space Sci.*, 18, 1659–1661, 1970a.
- Lebedinets, V. N. and Shushkova, V. B.: Micrometeorite Sputtering in Ionosphere, *Planet. Space Sci.*, 18, 1653–1661, 1970b.
- Lide, D. R: CRC Handbook of Chemistry and Physics, CRC Press, Boca Raton, 4-152 and 10-215, 1993.
- Lodders, S. G. and Fegley, J. B.: *The Planetary Scientist's Companion*, Oxford University Press, New York, 371 pp., 1988.
- Love, S. G. and Brownlee, D. E.: Heating and Thermal Transformation of Micrometeoroids Entering the Earth's Atmosphere, *Icarus*, 89, 26–43, 1991.
- Love, S. G. and Brownlee, D. E.: A Direct Measurement of the Terrestrial Mass Accretion Rate of Cosmic Dust, *Science*, 262, 550–553, 1993.
- Love, S. G., Brownlee, D. E., King, N. L., and Horz, F.: Morphology of Meteoroid and Debris Impact Craters Formed in Soft Metal Targets on the LDEF Satellite, *Int. J. Impact Engng.*, 16, 405–418, 1995.
- Love, S. G., Joswiak, D. J., and Brownlee, D. E.: Densities of 5-15 μm interplanetary dust particles, 901–902, Lunar and Planetary Institute, Houston, USA, 1993.
- Love, S. G., Joswiak, D. J., and Brownlee, D. E.: Densities of stratospheric micrometeorites, *Icarus*, 111, 227–236, 1994.
- Markova, O. M., Yakovlev, O. I., Semenov, G. A., and Belov, A. N.: Evaporation of natural melts in a Knudsen chamber, *Geokhimiya*, 11, 1559–1568, 1986.
- Mason, B.: *Handbook of Elemental Abundances of the Elements in Meteorites*, Gordon and Breach, Newark, 1971.
- Mathews, J. D., Janches, D., Meisel, D. D., and Zhou, Q. H.: The micrometeoroid mass flux into the upper atmosphere: Arecibo results and a comparison with prior estimates, *Geophys. Res. Lett.*, 28, 1929–1932, 2001.

Meteoric ablation

T. Vondrak et al.

[Title Page](#)[Abstract](#)[Introduction](#)[Conclusions](#)[References](#)[Tables](#)[Figures](#)[◀](#)[▶](#)[◀](#)[▶](#)[Back](#)[Close](#)[Full Screen / Esc](#)[Printer-friendly Version](#)[Interactive Discussion](#)

Meteoritic ablation

T. Vondrak et al.

[Title Page](#)[Abstract](#)[Introduction](#)[Conclusions](#)[References](#)[Tables](#)[Figures](#)[◀](#)[▶](#)[◀](#)[▶](#)[Back](#)[Close](#)[Full Screen / Esc](#)[Printer-friendly Version](#)[Interactive Discussion](#)

Matsunami, N., Yamamura, Y., Itikawa, Y., Itoh, N., Kazumata, Y., Miyagawa, S., Morita, K., and Shimizu, R.: A Semi-Empirical Formula for the Energy-Dependence of the Sputtering Yield, *Radiat. Eff. Lett.*, 57, 15–21, 1980.

McBride, N., Green, S. F., and McDonnell, J. A. M.: Meteoroids and small sized debris in Low Earth Orbit and at 1 au: Results of recent modelling, *Adv. Space Res.*, 23, 73–82, 1999.

McKinley, D. W. R.: *Meteor Science and Engineering*, McGraw-Hill, New York, 172–183, 1961.

McNeil, W. J., Lai, S. T., and Murad, E.: Differential ablation of cosmic dust and implications for the relative abundances of atmospheric metals, *J. Geophys. Res.*, 103, 10899–10911, 1998.

McNeil, W. J., Murad, E., and Lai, S. T.: Comprehensive Model for the Atmospheric Sodium Layer, *J. Geophys. Res.*, 100, 16847–16855, 1995.

Megner, L., Rapp, M., and Gumbel, J.: Distribution of meteoric smoke - sensitivity to micro-physical properties and atmospheric conditions, *Atmos. Chem. Phys.*, 6, 4415–4426, 2006, <http://www.atmos-chem-phys.net/6/4415/2006/>.

Opik, E. J.: *Physics of Meteor Flight in the Atmosphere*, Interscience, London, 1958.

Pellinen-Wannberg, A. and Wannberg, G.: Meteor observations with the European incoherent scatter UHF radar, *J. Geophys. Res.*, 99, 11379–11390, 1994.

Plane, J. M. C.: The Chemistry of Meteoric Metals in the Earth's Upper-Atmosphere, *Int. Rev. Phys. Chem.*, 10, 55–106, 1991.

Plane, J. M. C.: Atmospheric chemistry of meteoric metals, *Chem. Rev.*, 103, 4963–4984, 2003.

Plane, J. M. C.: A time-resolved model of the mesospheric Na layer: constraints on the meteor input function, *Atmos. Chem. Phys.*, 4, 627–638, 2004, <http://www.atmos-chem-phys.net/4/627/2004/>.

Press, W. H., Teukolsky, S. A., Vetterling, W. T., and Flannery, B. P.: *Numerical Recipes in Fortran 77, The Art of Scientific Computing 2nd ed.*, Cambridge University Press, Cambridge, 547–577, 1992.

Qian, J. and Gardner, C. S.: Simultaneous lidar measurements of mesospheric Ca, Na, and temperature profiles at Urbana, Illinois, *J. Geophys. Res.*, 100, 7453–7470, 1995.

Rietmeijer, F. J. M.: Interrelationships among meteoric metals, meteors, interplanetary dust, micrometeorites, and meteorites, *Meteoritics Planet Sci.*, 35, 1025–1041, 2000.

Rietmeijer, F. J. M.: Collected Extraterrestrial Materials: Intrplanetary Dust Particles, Micrometeorites, Meteorites, and Meteoric Dust, in: *Meteors in the Earth's Atmosphere*, edited by:

Meteoric ablation

T. Vondrak et al.

[Title Page](#)[Abstract](#)[Introduction](#)[Conclusions](#)[References](#)[Tables](#)[Figures](#)[◀](#)[▶](#)[◀](#)[▶](#)[Back](#)[Close](#)[Full Screen / Esc](#)[Printer-friendly Version](#)[Interactive Discussion](#)

- Williams, I. P. and Murad, E., 215–245, Cambridge University Press, Cambridge, 2002.
- Rogers, L. A., Hill, K. A., and Hawkes, R. L.: Mass loss due to sputtering and thermal processes in meteoroid ablation, *Planet. Space Sci.*, 53, 1341–1354, 2005.
- Saunders, R. W. and Plane, J. M. C.: A laboratory study of meteor smoke analogues: Composition, optical properties and growth kinetics, *J. Atmos. Solar-Terr. Phys.*, 68, 2182–2202, 2006.
- Schaefer, L. and Fegley, B.: A thermodynamic model of high temperature lava vaporization on Io, *Icarus*, 169, 216–241, 2004.
- Schaefer, L. and Fegley, B.: Application of an equilibrium vaporization model to the ablation of chondritic and achondritic meteoroids, *Earth Moon Planets*, 95, 413–423, 2005.
- Sears, D. W. and Dodd, R. T.: Overview and Classification of Meteorites, in *Meteorites and the Early Solar System*, edited by: Kerridge, J. F. and Matthews, M. S., University of Arizona Press, Tucson, 1988.
- Sigmund, P.: *Sputtering by Particle Bombardment* Springer-Verlag, Berlin, 9–71, 1981.
- Sigurðsson, H., Stix, J., Houghton, B., McNutt, S. R., and Rymer, H.: *Encyclopedia of Volcanoes* Academic Press, London, 186–188, 2000.
- Taylor, S., Lever, J. H., and Harvey, R. P.: Numbers, types, and compositions of and unbiased collection of cosmic spehrules, *Meteoritics Planetary Sci.*, 35, 651–666, 2000.
- Tielens, A. G. G. M., Mckee, C. F., Seab, C. G., and Hollenbach, D. J.: The Physics of Grain-Grain Collisions and Gas-Grain Sputtering in Interstellar Shocks, *Astrophys. J.*, 431, 321–340, 1994.
- von Zahn, U., Gerding, M., Hoffner, J., McNeil, W. J., and Murad, E.: Iron, calcium, and potassium atom densities in the trails of Leonids and other meteors: Strong evidence for differential ablation, *Meteoritics Planet. Sci.*, 34, 1017–1027, 1999.
- von Zahn, U., Hoffner, J., and McNeil, W. J.: Meteor trails as observed by Iidar, in *Meteors in the earth's atmosphere*, edited by E. Murad and I. P. Williams, pp. 149–187, Cambridge University Press, Cambridge, 149–187, 2002.
- Williams, I. P.: The evolution of meteoroid streams, in: *Meteors in the earth's atmosphere*, edited by: Murad, E. and Williams, I. P., 2–32, Cambridge University Press, Cambridge, 2002.
- Yamamura, Y., Matsunami, N., and Itoh, N.: Theoretical-Studies on an Empirical-Formula for Sputtering Yield at Normal Incidence, *Radiat. Eff. Defect. S.*, 71, 65–86, 1983.

Meteoric ablation

T. Vondrak et al.

Table 1. Parameters used in the chemical ablation model (CAMOD).

Free molecular drag coefficient, Γ	1.0 (Hughes, 1978)
Meteoroid density, ρ_m	0.3, 1.0, 2.0, 3.0, or $3.5 \times 10^3 \text{ kg m}^{-3}$
Molecular heat transfer coefficient, Λ	1.0
Emissivity, ε	1.0
Temperature of environment, T_{env}	200 K
Specific heat of meteoroid, C	$1 \times 10^3 \text{ J kg}^{-1} \text{ K}^{-1}$
Latent heat of vaporisation, L	$(3.0 \text{ or } 6.0) \times 10^6 \text{ J kg}^{-1}$
Impact angle, χ	37° or 0°
Uptake coefficient, γ	1.0*
Surface binding energy, U_0	5.7 eV (Tielens et al., 1994)
Material constant (silicate), K	0.1 (Tielens et al., 1994)

* The value of sticking coefficient is set to 0 for temperatures below 1700 K, 0.5 for 1800 K and 1 for temperatures higher than 1900 K. Within this interval the values follow a *sigmoid* curve (see Fig. 4a).

Title Page

Abstract

Introduction

Conclusions

References

Tables

Figures

◀

▶

◀

▶

Back

Close

Full Screen / Esc

Printer-friendly Version

Interactive Discussion



Meteoric ablation

T. Vondrak et al.

Table 2. Initial composition of meteoroids (Mason, 1971; Fegley and Cameron, 1987; Lodders and Fegley, 1988; Sears and Dodd, 1988).

Oxide	Oxide mass%	Elemental abundance ^a	Elemental atomic%
SiO ₂	34.0	1.00×10 ⁶	13.6
MgO	24.2	1.06×10 ⁶	14.4
FeO	36.3	8.91×10 ⁵	12.1
Al ₂ O ₃	2.5	8.50×10 ⁴	1.2
CaO	1.9	6.01×10 ⁴	8.2×10 ⁻¹
Na ₂ O	1.0	5.90×10 ⁴	8.0×10 ⁻¹
K ₂ O	0.1	3.77×10 ³	5.1×10 ⁻²
TiO ₂	0.01	2.65×10 ²	3.6×10 ⁻³

^a Elemental abundance on the cosmochemical scale: Si is taken as 1.00×10⁶.

[Title Page](#)
[Abstract](#)
[Introduction](#)
[Conclusions](#)
[References](#)
[Tables](#)
[Figures](#)
[Back](#)
[Close](#)
[Full Screen / Esc](#)
[Printer-friendly Version](#)
[Interactive Discussion](#)


Meteoric ablation

T. Vondrak et al.

Table 3. Ablated fraction and the ablation profile parameters (centroid height and FWHM) for ablation of the major elements from the most probable meteoroid (mass=5 μg , entry velocity=20.5 km s^{-1} , $\chi=37^\circ$, $\rho_m=2.0 \text{ g cm}^{-3}$)

Element	Ablated fraction atomic%	Centroid height km	FWHM ^a km
Si	93.8	86.8	6.5
Mg	93.2	85.3	4.1
Fe	100.0	88.9	5.3
Ca	0.6	84.6	3.7
Al	0.2	86.7	4.0
Ti	4.0	85.0	5.3
Na	100.0	98.6	0.8
K	100.0	98.3	0.4
O	90.8	87.0	6.9

^a FWHM: full-width-at-half-maximum.

[Title Page](#)
[Abstract](#)
[Introduction](#)
[Conclusions](#)
[References](#)
[Tables](#)
[Figures](#)
[I◀](#)
[▶I](#)
[◀](#)
[▶](#)
[Back](#)
[Close](#)
[Full Screen / Esc](#)
[Printer-friendly Version](#)
[Interactive Discussion](#)


Meteoric ablation

T. Vondrak et al.

Table 4. Ablated fraction and the ablation profile parameters (centroid height and FWHM) for ablation of the major elements from meteoroids integrated over the whole mass and velocity distribution.

Zenith angle:		37°		0°		
Element	Ablated fraction atomic%	Centroid height km	FWHM ^a km	Ablated fraction atomic%	Centroid height km	FWHM ^a km
Si	59.5	84.6	16.6	64.1	83.9	16.7
Mg	54.0	83.3	16.4	58.6	83.8	16.9
Fe	71.3	85.5	17.5	75.6	82.4	17
Ca	22.9	82.3	15.7	25.8	81.1	15.8
Al	7.5	82.5	13.2	9	81.2	13.5
Ti	22.8	82.3	14.2	26.1	81.3	14.1
Na	92.4	94	13.5	94.5	93.5	13
K	92.2	93.8	15.1	94.2	93.2	12.8
O	58.7	84.6	16.8	63.2	81.3	16.9

^a FWHM: full-width-at-half-maximum.

[Title Page](#)
[Abstract](#)
[Introduction](#)
[Conclusions](#)
[References](#)
[Tables](#)
[Figures](#)
[Back](#)
[Close](#)
[Full Screen / Esc](#)
[Printer-friendly Version](#)
[Interactive Discussion](#)


Meteoric ablation

T. Vondrak et al.

Table 5. Dependence of the elemental ablated fractions and centroid heights on the heat of vaporisation (L) for a meteoroid density 2 g cm^{-3} .

Heat of Ablation / MJ kg^{-1}	Ablated fraction atomic%		Centroid height km	
	3.0	6.0	3.0	6.0
Element				
Si	62.3	59.5	85.4	84.6
Mg	57.8	54.0	84.2	83.3
Fe	72.4	71.3	86.2	85.5
Ca	26.8	22.9	83.4	82.3
Na	92.5	92.4	94.2	94.0
K	92.2	92.2	93.9	93.8

[Title Page](#)
[Abstract](#)
[Introduction](#)
[Conclusions](#)
[References](#)
[Tables](#)
[Figures](#)
[Back](#)
[Close](#)
[Full Screen / Esc](#)
[Printer-friendly Version](#)
[Interactive Discussion](#)


Meteoric ablation

T. Vondrak et al.

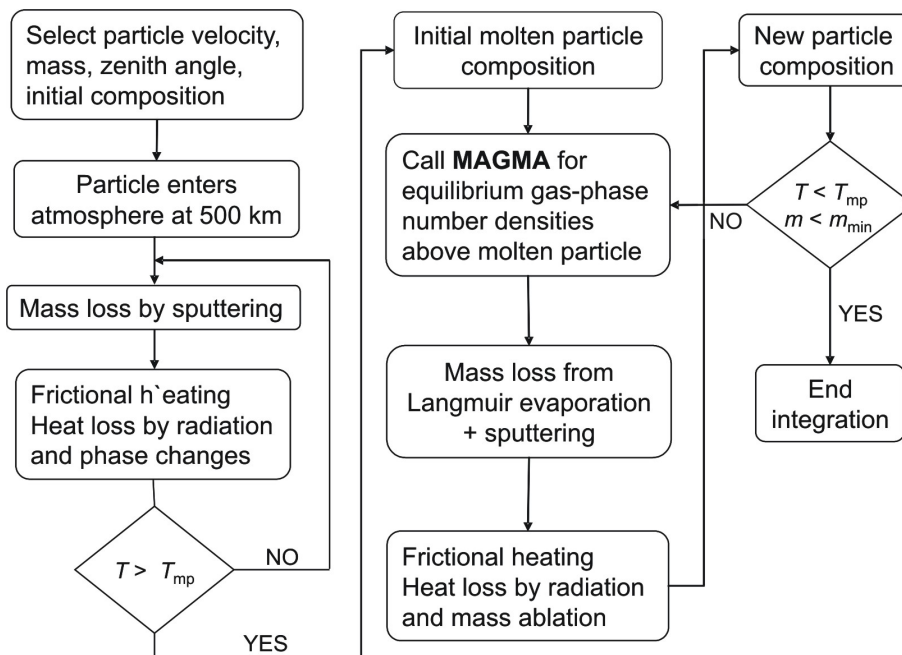


Fig. 1. Flow chart illustrating the architecture of the chemical ablation model.

[Title Page](#)
[Abstract](#)
[Introduction](#)
[Conclusions](#)
[References](#)
[Tables](#)
[Figures](#)
[◀](#)
[▶](#)
[◀](#)
[▶](#)
[Back](#)
[Close](#)
[Full Screen / Esc](#)
[Printer-friendly Version](#)
[Interactive Discussion](#)

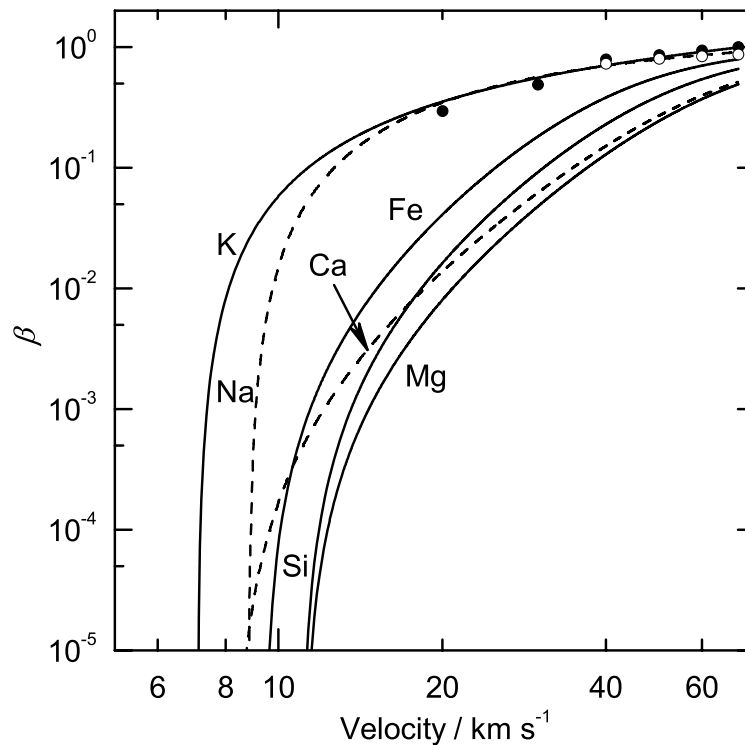



Fig. 2. Ionization coefficient of the elements. (●) Experimental values for K–N₂ collisions (Cuderman, 1972). The line through the points is a least-squares fit $0.347(V - V_0)^2 V^{-1.702}$. (○) Experimental values for Na – N₂ collisions (Bydin and Bukhteev, 1960). The dashed line is a least squares fit $0.933(V - V_0)^2 V^{-1.94}$.

[Title Page](#)
[Abstract](#)
[Introduction](#)
[Conclusions](#)
[References](#)
[Tables](#)
[Figures](#)
[◀](#)
[▶](#)
[◀](#)
[▶](#)
[Back](#)
[Close](#)
[Full Screen / Esc](#)
[Printer-friendly Version](#)
[Interactive Discussion](#)


Meteoric ablation

T. Vondrak et al.

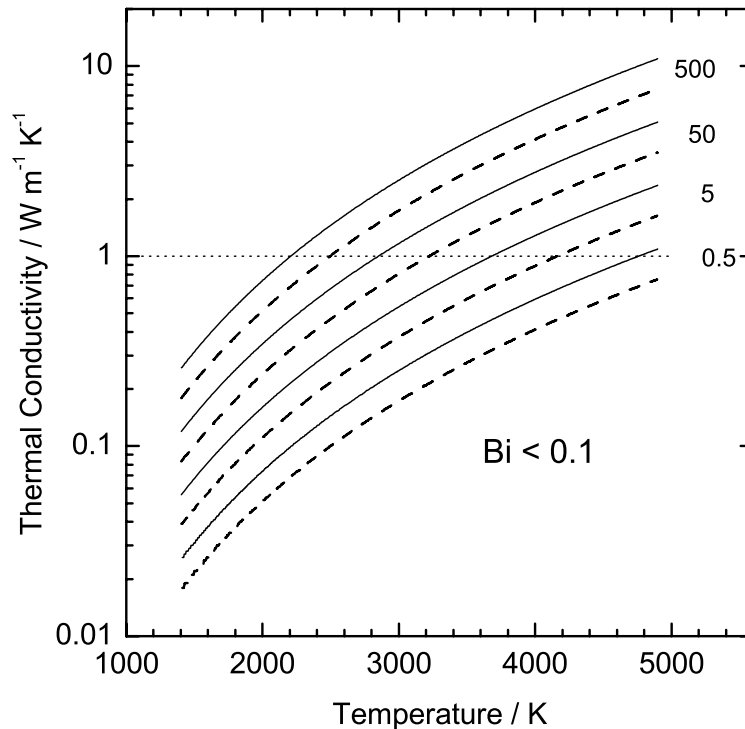


Fig. 3. Heat transport in the meteoroid. The dependence of the isothermicity condition on the ablation temperatures, for a range of particle masses (0.5 to 500 μg) and particle densities (solid lines 1 g cm^{-3} , broken lines 3 g cm^{-3}). For the points below the curves the Biot number is lower than 0.1 and thus the isothermicity condition is fulfilled. The dotted line marks the thermal conductivity of olivine.

[Title Page](#)
[Abstract](#)
[Introduction](#)
[Conclusions](#)
[References](#)
[Tables](#)
[Figures](#)
[◀](#)
[▶](#)
[◀](#)
[▶](#)
[Back](#)
[Close](#)
[Full Screen / Esc](#)
[Printer-friendly Version](#)
[Interactive Discussion](#)

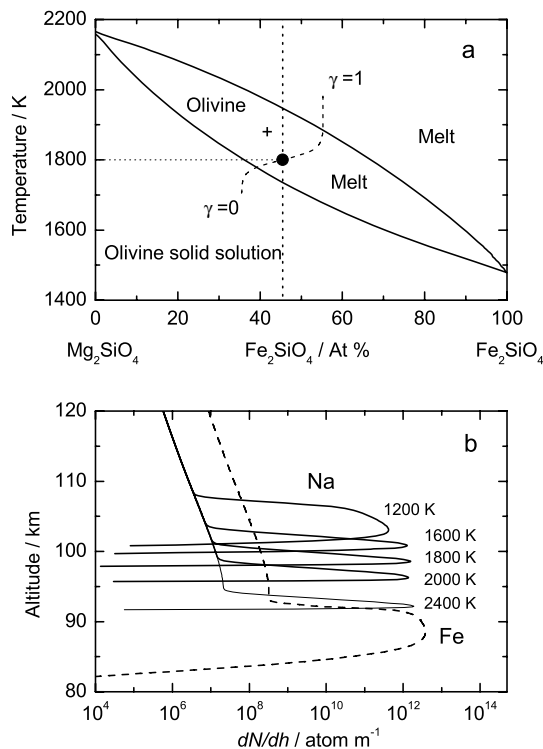



Fig. 4. Melting temperature of the meteoroid. **(a)** Phase diagram of olivine and the assumed melting temperature of the chondritic particle. The dashed line represents the temperature dependence of the uptake coefficient γ , which is used to implement a smooth melting transition in the model. **(b)** The dependence of the Na ablation profile (solid lines) on the meteoroid melting temperature, for a $5 \mu\text{g}$ meteoroid at 20 km s^{-1} . The Fe ablation profile (broken line) for 1800 K is shown for comparison.

[Title Page](#)
[Abstract](#)
[Introduction](#)
[Conclusions](#)
[References](#)
[Tables](#)
[Figures](#)
[◀](#)
[▶](#)
[◀](#)
[▶](#)
[Back](#)
[Close](#)
[Full Screen / Esc](#)
[Printer-friendly Version](#)
[Interactive Discussion](#)


Meteoric ablation

T. Vondrak et al.

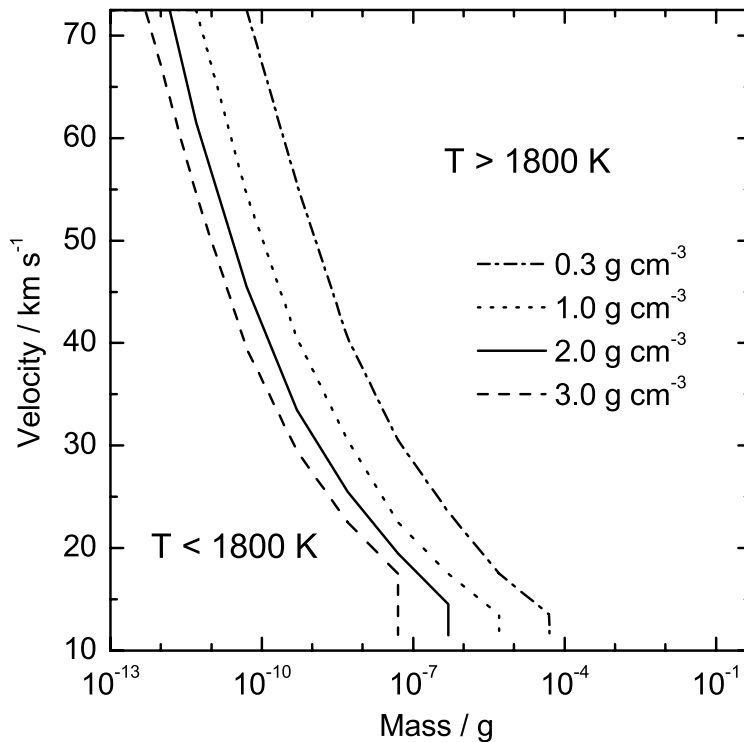


Fig. 5. Dependence of the thermal ablation threshold on meteoroid mass and velocity for a range of particle densities ($0.3\text{--}3\text{ g cm}^{-3}$). Only particles to the right of the curves reach a temperature greater than 1800 K.

[Title Page](#)[Abstract](#)[Introduction](#)[Conclusions](#)[References](#)[Tables](#)[Figures](#)[◀](#)[▶](#)[◀](#)[▶](#)[Back](#)[Close](#)[Full Screen / Esc](#)[Printer-friendly Version](#)[Interactive Discussion](#)

Meteoric ablation

T. Vondrak et al.

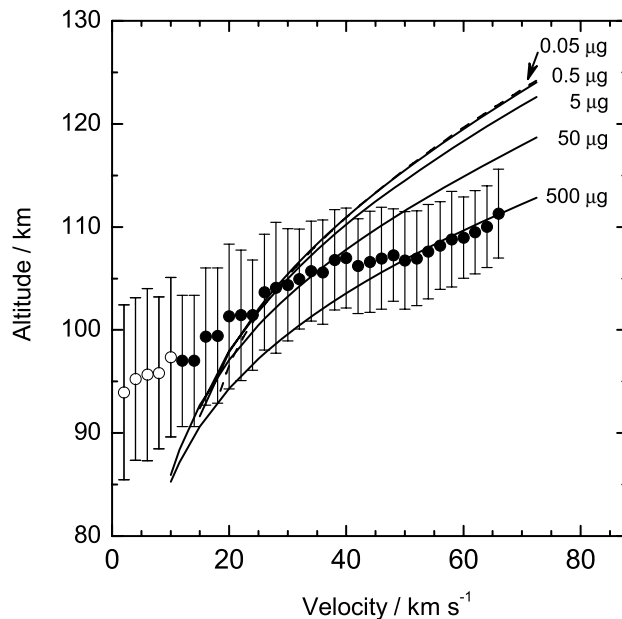


Fig. 6. Comparison of the average appearance heights of meteor head echoes observed by the 430 MHz radar at Arecibo as a function of entry velocity (points, with 1σ standard deviations), and the modelled appearance heights (lines) defined as the altitude when the particle temperature reaches 1800 K and the alkali metals start to ablate thermally, for a range of particle masses (0.05–500 μg). The recorded velocities lower than 10 km s^{-1} (hollow points) correspond to particles arriving at large entry angles, which therefore have a small vertical velocity component.

[Title Page](#)[Abstract](#)[Introduction](#)[Conclusions](#)[References](#)[Tables](#)[Figures](#)[◀](#)[▶](#)[◀](#)[▶](#)[Back](#)[Close](#)[Full Screen / Esc](#)[Printer-friendly Version](#)[Interactive Discussion](#)

Meteoric ablation

T. Vondrak et al.

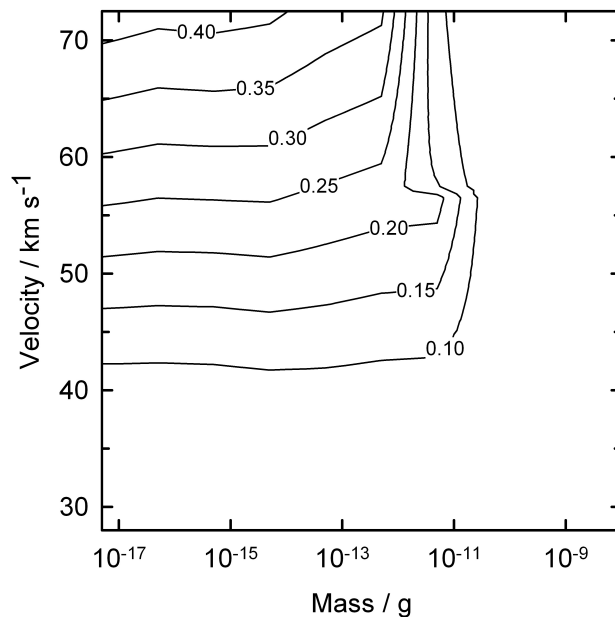


Fig. 7. Non-thermal mass loss. The fraction of a particle sputtered before it reaches 1700 K, as a function of meteoroid mass and velocity. Meteoroids smaller than $\sim 10^{-13}$ g do not reach the melting temperature (1800 K), so the sputtered fraction is the whole mass loss. Particle density = 2 g cm^{-3} .

[Title Page](#)[Abstract](#)[Introduction](#)[Conclusions](#)[References](#)[Tables](#)[Figures](#)[◀](#)[▶](#)[◀](#)[▶](#)[Back](#)[Close](#)[Full Screen / Esc](#)[Printer-friendly Version](#)[Interactive Discussion](#)

Meteoric ablation

T. Vondrak et al.

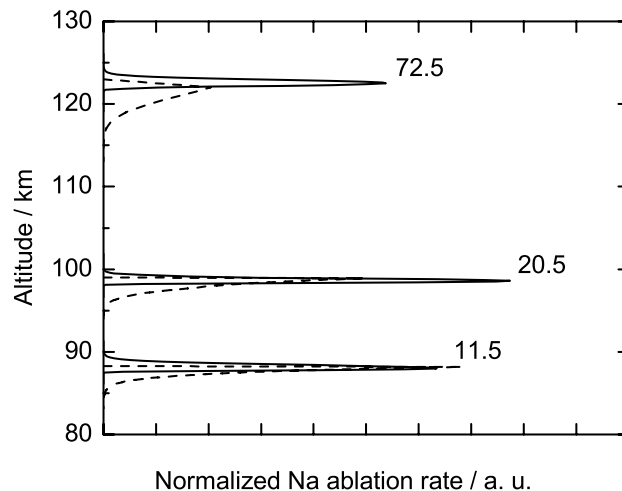


Fig. 8. Radial diffusion compared with Langmuir evaporation. The rate of Na ablation assuming unrestricted Langmuir evaporation from a $5\ \mu\text{g}$ meteoroid (solid lines), compared with the ablation rate assuming diffusion control of Na through the molten particle (broken lines), for three different meteoroid velocities (in km s^{-1}).

[Title Page](#)[Abstract](#)[Introduction](#)[Conclusions](#)[References](#)[Tables](#)[Figures](#)[◀](#)[▶](#)[◀](#)[▶](#)[Back](#)[Close](#)[Full Screen / Esc](#)[Printer-friendly Version](#)[Interactive Discussion](#)

Meteoric ablation

T. Vondrak et al.

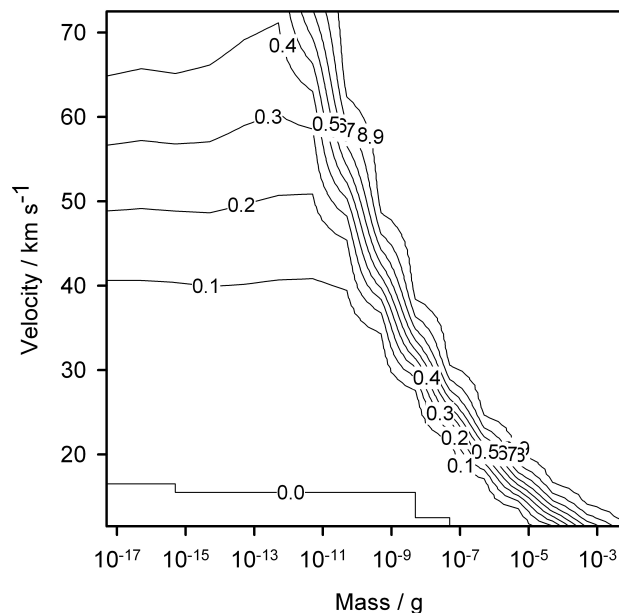


Fig. 9. Ablated fraction of a meteoroid (particle density 2 g cm^{-3}), as a function of mass and velocity (the wavy structure of the contours is an artefact caused by the discretisation of the particle mass distribution).

[Title Page](#)[Abstract](#)[Introduction](#)[Conclusions](#)[References](#)[Tables](#)[Figures](#)[◀](#)[▶](#)[◀](#)[▶](#)[Back](#)[Close](#)[Full Screen / Esc](#)[Printer-friendly Version](#)[Interactive Discussion](#)

Meteoric ablation

T. Vondrak et al.

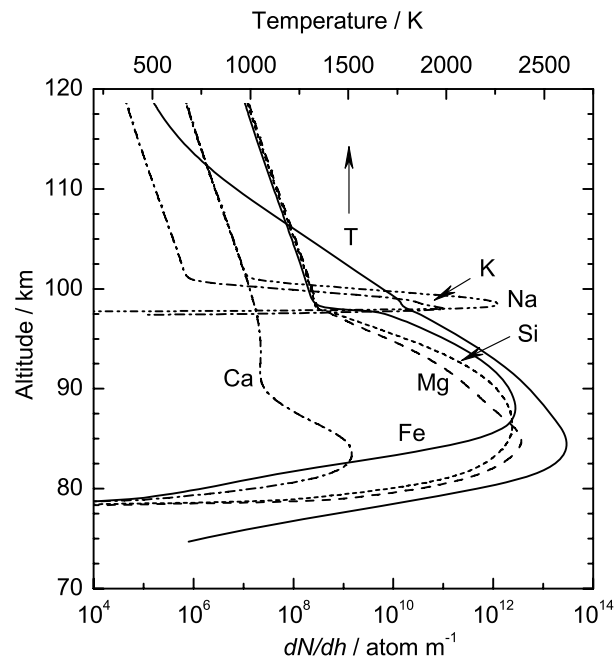


Fig. 10. Ablation profiles of individual elements from a $5 \mu\text{g}$ meteoroid entering at 20 km s^{-1} . The particle temperature is shown with the solid line, referenced to the top abscissa.

[Title Page](#)[Abstract](#)[Introduction](#)[Conclusions](#)[References](#)[Tables](#)[Figures](#)[◀](#)[▶](#)[◀](#)[▶](#)[Back](#)[Close](#)[Full Screen / Esc](#)[Printer-friendly Version](#)[Interactive Discussion](#)

Meteoric ablation

T. Vondrak et al.

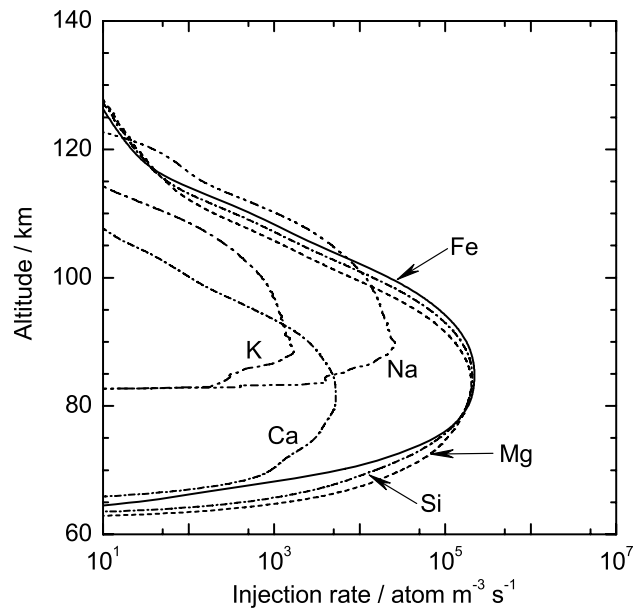


Fig. 11. Injection rates of individual elements, integrated over the LDEF distributions of meteoroid mass (5×10^{-18} – 5×10^{-3} g) and velocity (11.5 – 72.5 km s $^{-1}$). Note that these injection rates should be scaled by a factor of 0.34 if the total mass flux is 30 t d $^{-1}$ (see text).

[Title Page](#)[Abstract](#)[Introduction](#)[Conclusions](#)[References](#)[Tables](#)[Figures](#)[◀](#)[▶](#)[◀](#)[▶](#)[Back](#)[Close](#)[Full Screen / Esc](#)[Printer-friendly Version](#)[Interactive Discussion](#)

Meteoric ablation

T. Vondrak et al.

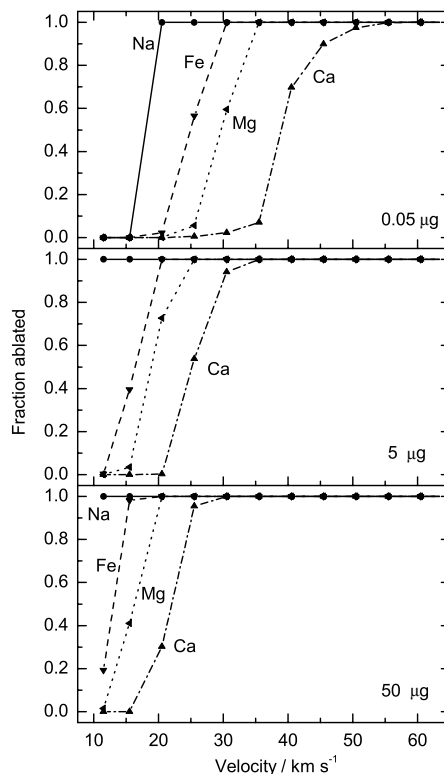


Fig. 12. Dependence of elemental ablation on the particle density. The ablated fraction of the initial mass (upper panel) and centroid of the ablation profile (lower panel) are shown for selected elements, integrated over the LDEF distributions of mass (5×10^{-18} – 5×10^{-3} g) and velocity (11.5 – 72.5 km s $^{-1}$). The dashed vertical line indicates the particle density inferred from the analysis of impact craters in the LDEF experiment.

[Title Page](#)
[Abstract](#)
[Introduction](#)
[Conclusions](#)
[References](#)
[Tables](#)
[Figures](#)
[◀](#)
[▶](#)
[◀](#)
[▶](#)
[Back](#)
[Close](#)
[Full Screen / Esc](#)
[Printer-friendly Version](#)
[Interactive Discussion](#)


Meteoric ablation

T. Vondrak et al.

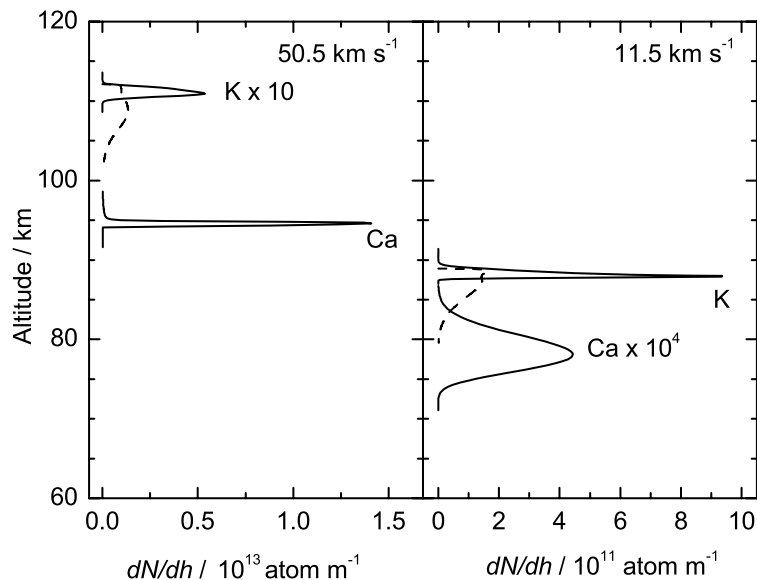


Fig. 13. Ablation of Ca and K from a 50 μg meteoroid with an initial velocity of 50.5 km s^{-1} (left panel), and 11.5 km s^{-1} (right panel). The dashed lines indicate the diffusion-controlled release of K, the solid lines correspond to ablation rates calculated assuming Langmuir evaporation is rate-limiting.

[Title Page](#)[Abstract](#)[Introduction](#)[Conclusions](#)[References](#)[Tables](#)[Figures](#)[◀](#)[▶](#)[◀](#)[▶](#)[Back](#)[Close](#)[Full Screen / Esc](#)[Printer-friendly Version](#)[Interactive Discussion](#)

Meteoric ablation

T. Vondrak et al.

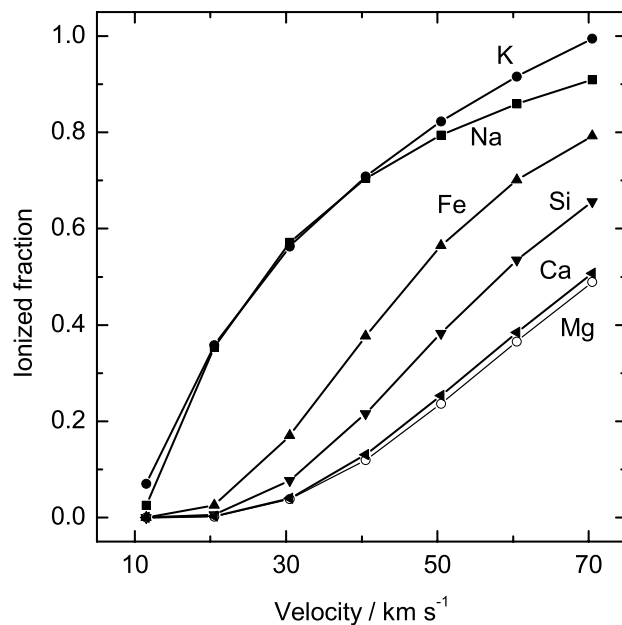


Fig. 14. Dependence of the ionized fraction β of selected elements (at their peak ablation altitude) on the initial velocity of a $5 \mu\text{g}$ meteoroid.

[Title Page](#)[Abstract](#)[Introduction](#)[Conclusions](#)[References](#)[Tables](#)[Figures](#)[◀](#)[▶](#)[◀](#)[▶](#)[Back](#)[Close](#)[Full Screen / Esc](#)[Printer-friendly Version](#)[Interactive Discussion](#)

Meteoric ablation

T. Vondrak et al.

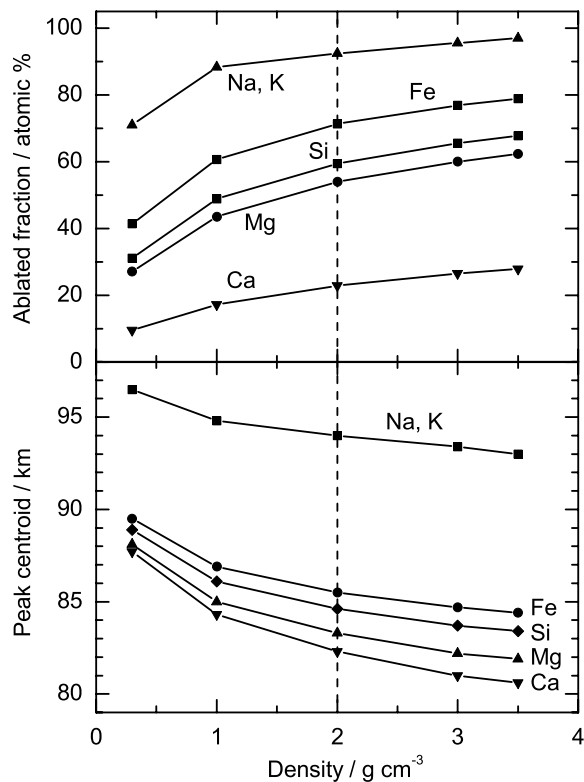


Fig. 15. Dependence of the ablated fraction of Na, Fe, Mg and Ca on meteoroid velocity for 0.05 μg , 5 μg , and 50 μg particles.

[Title Page](#)[Abstract](#)[Introduction](#)[Conclusions](#)[References](#)[Tables](#)[Figures](#)[◀](#)[▶](#)[◀](#)[▶](#)[Back](#)[Close](#)[Full Screen / Esc](#)[Printer-friendly Version](#)[Interactive Discussion](#)